Supplemental Materials

Supplemental Methods

Cell Culture and Treatment

Thoracic aortas were digested for 5 min at 37 °C in HBSS containing 1 mg/ml collagenase A (10103578001, Sigma-Aldrich) to promote sharp removal of the adventitia under a dissecting microscope. The denuded vessels were transferred into 0.5 ml DMEM (Thermo Fisher) containing 10% FBS (Life Technologies), 1.5 mg/ml collagenase A, and 0.5 mg/ml elastase (LS006365, Worthington) and incubated at 37 °C for 30 min while the digest was triturated with a pipette every 15 min. The mixture was centrifuged, then the cells were resuspended in Claycomb medium (Sigma-Aldrich) supplemented with 10% FBS, and cultured in 35 mm dishes in a CO_2 incubator at 37 °C. On reaching confluence, the cells were dissociated with trypsin/EDTA and GFP^+ SMCs were sorted under sterile conditions using a FACSAria (BD Biosciences). The selected cells were expanded and used for experiments at passage 2 or 3. Signaling studies were performed after resting the SMCs in DMEM with 0.1% FBS for 72 h or 12 h for treatment with Wnt3a (R&D) and rapamycin (Calbiochem) at the indicated doses and times. Synthetic siRNAs (*Mitf* L-047441-00-0005, *Ctnnb1* L-040628-00-0005, and Non-targeting Control Pool D-001810-10, Dharmacon) were transfected using Lipofectamine RNAiMax (Thermo Fisher) and the effects of gene knockdown were analyzed after 72 h.

Elastin Deposition

0.5×10^5 GFP^+ SMCs from thoracic aortas of 3 week-old mice were plated on gelatin-coated cover slips in 12-well plates and cultured in DMEM with 10% FBS for 4 d. The cells were rinsed twice with phosphate-buffered saline (PBS) and fixed with 4% PFA. Elastin was visualized using an antibody to mouse recombinant tropoelastin exons 6-17 that detects both mature and immature elastin[1] (1:400, gift of Robert P. Mecham, Washington University). Additionally, cell cultures were stained with antibodies to human fibrillin-1 (cross-reactive with mouse, 1:100, ab53076, Abcam) and mouse MAGP-1[2], a fibrillin-associated protein (1:100, gift of Robert P. Mecham, Washington University).

Elastin Degradation

Ascending aortas without TAAD from 12 week-old mice were embedded in OCT and sectioned at 5 µm. The slides were incubated in 30 µg/ml elastase (LS006365, Worthington) for 30 min at 37 °C. Elastic fibers were labeled with Alexa Fluor 633 hydrazide (Thermo Fisher) at 0.6 µM overnight at 4 °C. Sections were mounted with ProLong Gold Antifade reagent with DAPI and imaged using an Axiovert 200M fluorescence imaging microscope (Zeiss).

Elastase Activity

Thoracic aortas of 24 week-old mice were digested in Cell Lysis Buffer (Cell Signaling). Protein concentration was measured by Pierce BCA Protein Assay Kit (Thermo Fisher) and equal amounts of protein were mixed with DQ-elastin labeled with BODIPY FL dye (E12056, Thermo Fisher). Fluorescence intensity was measured following incubation of the reaction in the dark for 2-12 h at room temperature.

MMP Activity

For fluorescence imaging, MMPSense 645 FAST (NEV10100, PerkinElmer) was injected i.v. at 4 nmol per dose at 72 and 36 h prior to euthanasia of 12 and 24 week-old mice. Cells were isolated from the ascending and proximal descending aorta and analyzed by flow cytometry. For gel zymography, 1×10^6 GFP^+ SMCs were seeded in 6-well plates in DMEM with 0.1% FBS for 72 h. The supernatant was concentrated 10-fold using a Protein Concentrator (Thermo Fisher). Protein was extracted from cells in Cell Lysis Buffer (Cell Signaling) and the concentration measured by Pierce BCA Protein Assay Kit (Thermo Fisher). Equal volumes of supernatant or amounts of protein per sample were mixed with loading buffer and loaded to 10% acrylamide gels containing 0.1% gelatin as a substrate. After electrophoresis, the gels were incubated in

Zymogram Renaturation Buffer (Bio-Rad) for 1 h, equilibrated in Zymogram Development Buffer (Bio-Rad) for 24 h, and stained with SimplyBlue SafeStain (Thermo Fisher).

Flow Cytometry

Thoracic aortas were procured, rinsed in cold PBS, opened longitudinally, and sliced into small fragments around 3 mm in size. The minced tissue was incubated in 0.5 ml DMEM with 10% FBS, 1.5 mg/ml collagenase A, and 0.5 mg/ml elastase for 60 min at 37 °C while the tissue fragments were gently triturated using a pipette every 15 min. The digested aorta solution was passed through a 40 μm filter and incubated with cell-impermeant viability dye (65-0863-14 or 65-0865-14, Thermo Fisher) for 20 min, fixed with Fixation Buffer (eBioscience) for 15 min, washed, resuspended in Permeabilization Buffer (eBioscience), and blocked with unconjugated Fc antibodies (Biolegend, except when staining for CD16/32) for 20 min, all at 4 °C. The cells were stained with DAPI (1:5000, 564907, BD Biosciences) or antibodies to p-HH3 (1:100, 50-9124-42, Thermo Fisher), MMP2 (1:2000, ab37150, Abcam), LAMP2 (1:200, 743181 or 564843, BD Biosciences), GAL3 (1:200, 125416 or 125408, BioLegend), CD68 (1:100, 137017 or 137003, BioLegend), CD11b (1:100, 562605 or 561690, BD Biosciences), CD45 (1:100, 109831 or 109817, BioLegend), F4/80 (1:100, 123121, BioLegend), CD16/32 (1:100, 101314, BioLegend), GFP (1:200, 565197, BD Biosciences), and SMA (1:200, F3777, Sigma-Aldridge or 1:200, IC1420R, R&D) or isotype-matched, irrelevant IgG control for 1 h on ice in the dark. The antibodies were directly conjugated except for MMP2, which was visualized with Alexa Fluor 647–conjugated IgG (Invitrogen). The cells were pelleted and resuspended in 0.4% BSA/PBS for analysis using a LSR II (BD Biosciences). Sequential gating was used to exclude: i) small debris and damaged cells by forward versus side scatter area, ii) doublets by side scatter followed by forward scatter width versus height, iii) non-viable cells by impermeant dye uptake, and iv) cells not of SMC origin by RFP expression or absence of GFP expression, with possible artifact from failed Cre recombination in a few SMCs. Fluorescence was detected in up to 5 channels (violet, green, red, far-red, and near-infrared) with multicolor compensation by fluorescence-minus-one gates. The data was analyzed with FlowJo software.

Lysosome Number and Function

At 60% confluency, GFP^+ SMCs were serum-deprived in DMEM with 0.1% FBS for 24 h and then treated with Lysotracker Deep Red (Thermo Fisher), diluted 1: 1,000 in prewarmed DMEM with 0.1% FBS, for 3 min or DQ Red BSA (Thermo Fisher) at 5 μg/ml for 14 h at 37 °C. The cells were briefly washed twice with prewarmed PBS, trypsinized, fixed in suspension with Fixation Buffer (eBioscience) for 15 min at room temperature, and analyzed by flow cytometry. Alternatively, GFP^+ SMCs were plated on gelatin-coated cover slips in 12-well plates and treated with Lysotracker Deep Red or DQ Red BSA as described above. The cells were fixed with 4% PFA for 10 min on ice in the dark and washed extensively with PBS. The cover slips were mounted with ProLong Gold Antifade reagent with DAPI (Life Technologies) and visualized using a SP5 confocal microscope (Leica).

Endocytosis and Lysosomal Degradation of Fibronectin

GFP^+ SMCs were seeded on 24-well plates in DMEM with 10% FBS for 1 h and then treated with 10 μg/ml of rhodamine-labeled fibronectin (FNR01, Cytoskeleton) in DMEM with 0.1% FBS for 6 h. The cells were briefly washed twice with prewarmed PBS and incubated in DMEM, 10% FBS, with or without 10 μM/ml of chloroquine (PHR1258, Sigma-Aldrich) for 6 h. Cells were then washed twice with PBS, dissociated with trypsin/EDTA, fixed in suspension with Fixation Buffer (eBioscience) for 15 min at room temperature, and analyzed by flow cytometry. Fibronectin uptake was calculated as rhodamine fluorescence in the presence of chloroquine (to prevent degradation of endolysosomal cargo) less background fluorescence of cells cultured without labeled matrix. Fibronectin degradation was calculated as the percent difference in rhodamine expression of cells cultured with or without chloroquine.

Uptake of Elastin

6-well plates were coated with rhodamine-labeled elastin particles < 37 μm size (RS144, Elastin Products Company) at 1 mg/ml in PBS for 2 h. Uncoated elastin was removed by washing in PBS repeated three times. 1×10^5 GFP^+ SMCs were initially added to the coated plates in DMEM with 10% FBS for 3 h, then further cultured in DMEM with 0.1% FBS for 72 h at 37 °C. The cells were dissociated with trypsin/EDTA and analyzed by flow cytometry. In certain experiments, rhodamine dim or bright populations of SMCs were separately sorted by flow cytometry and visualized by confocal microscopy after re-plating for 3 h in DMEM with 10% FBS.

Phagocytosis of Apoptotic Cells

Erythrocytes and leukocytes were isolated from whole blood by Ficoll gradient centrifugation and SMCs were isolated from adventitial-stripped thoracic aortas of C57BL/6J mice. The cells were labeled with PKH26 using a Red Fluorescent Cell Linker Kit (Sigma-Aldrich) according to the manufacturer's instructions. Apoptosis was induced by heat shock at 56 °C for 5 min. Labeled erythrocytes (3×10^6), leukocytes (1×10^5), or SMCs (0.5×10^5) were added to GFP^+ SMCs (1×10^5), previously plated on gelatin-coated cover slips in 12-well plates in DMEM with 0.1% FBS for 24 h, and co-cultured for 15 h at 37 °C. In certain experiments, GFP^+ SMCs were pretreated with neutralizing antibody to Axl (AF854, R&D), soluble Axl:Fc chimeric protein (7477AX050, R&D), or irrelevant antibody at 15 μg/ml for 1 h. Unengulfed non-adherent cells were removed by extensive washing in PBS and the adherent cells were either fixed and visualized by confocal microscopy or dissociated with trypsin/EDTA and analyzed by flow cytometry.

Biomechanical Assessment

Tissue preparation

Thoracic aortas were excised and separated into the ascending segment, from the aortic root to the brachiocephalic artery, and the descending thoracic segment, beginning immediately distal to the left subclavian artery and including the first 4-5 pairs of intercostal arteries. Perivascular tissue was removed gently and branches were ligated with 9-0 nylon suture.

Biaxial contractility assessment

Aortic segments were cannulated with custom-drawn glass pipets, mounted in a biaxial testing device[3], and maintained at 37 °C in an oxygenated (95% O_2 / 5% CO_2) Krebs-Ringer's solution (in mM: 123 NaCl, 4.7 KCl, 1.2 $MgCl_2$, 20 $NaHCO_3$, 1.2 KH_2PO_4, 5.6 glucose, and 2.5 $CaCl_2$). The geometry in a nearly unloaded state was defined as no axial load (i.e., axial stretch $\lambda_z = l/L$ = 1, where l is the loaded length and L the unloaded length) and a pressure P = 10 mmHg. To verify SMC viability, active preconditioning consisted of contracting the vessels for 15 min with 100 mM KCl, first at a low load (P = 40 mmHg; λ_z = 1.15) and then at a moderate load (P = 60 mmHg; λ_z = 1.30), values that were based on prior biomechanical tests[4-6]. Following preconditioning, the estimated in vivo axial stretch was determined by slowly ramping pressure from 80 to 100 mmHg and identifying the stretch at which the change in axial force was nearly zero. Vessels were then held fixed at their estimated in vivo axial stretch, pressurized to 90 mmHg, and stimulated with 100 mM KCl and then 1 μM phenylephrine. The testing chamber was flushed with fresh Krebs between each series of contractions to return the outer diameter to its original preconstricted value.

Passive biaxial testing

Passive biomechanical data were also collected as previously described[7,8]. Briefly, the testing chamber was drained and refilled with Hanks' buffered saline solution (HBSS) and maintained at room temperature to minimize smooth muscle contractility[9]. Unloaded geometry was determined and the passive in vivo axial stretch estimated as described above. Four passive preconditioning cycles were performed by ramping pressure from 10 to 140 mmHg at the estimated axial stretch to minimize viscoelastic contributions to the mechanical behavior. Three

pressure-diameter protocols consisted of cyclic pressurization from 10 to 140 mmHg while the vessel was held fixed at axial stretches of 95%, 100%, and 105% of the in vivo value, and four axial force-length protocols were performed by cyclically loading the vessels from 0 mN to f_{max} while maintaining distending pressure fixed at 10, 60, 100, and 140 mmHg. Values for f_{max} differed for the ascending and descending segments, again based on prior results[7,8]. Unloaded thickness was determined at the end of the protocol by cutting a ring from the segment and analyzing wall thickness using a custom MATLAB program as previously described[4].

Quantification of active properties

Contractile capacity was assessed as percent changes in outer diameter and mean circumferential stress, $\sigma_\vartheta = Pa/h$, between relaxed (basal) and contracted (active) states, with P the distending pressure, a the inner radius, and h the wall thickness, which can be computed from on-line measurements by enforcing incompressibility of the hydrated wall. Basal conditions correspond to maintenance in Krebs-Ringer's solution at 37 °C in the absence of vasostimulation and maximum contractility was defined at 15 min of stimulation. Although active circumferential force generation cannot be measured directly as is traditionally done with uniaxial ring or strip tests, average force can be calculated from the circumferential stress: $f_\vartheta = \sigma_\vartheta hl$, which allows comparisons with data from uniaxial tests, noting that our biaxial testing protocol is circumferentially isotonic (i.e., fixed load) not isometric (i.e., fixed geometry).

Quantification of passive mechanical properties

Passive mechanical properties were quantified as described previously[9]. Briefly, a nonlinear strain energy function W containing 8 material parameters (c, c_1^i, and c_2^i; $i = 1,2,3 = 4$) was used to fit biaxial data from the seven experimental protocols (pressure-diameter and axial force-length) using nonlinear regression, where

$$W(\mathbf{C}, \mathbf{M}^i) = \frac{c}{2}(I_\mathbf{C} - 3) + \sum_{i=1}^{4} \frac{c_1^i}{4c_2^i}\left\{exp\left[c_2^i\left(IV_\mathbf{C}^i - 1\right)^2\right] - 1\right\}$$

with $\mathbf{C}$ the right Cauchy-Green tensor determined from changes in geometry, $\mathbf{M}^i$ a unit vector denoting the direction of the i^{th} $\{i = 1,2,3 = 4\}$ family of locally parallel collagen fibers in a reference configuration, and $I_\mathbf{C}$ and $IV_\mathbf{C}$ coordinate invariant measures of the deformation. Cauchy wall stress and linearized biaxial material stiffness were determined via first and second derivatives of W, respectively, with respect to deformations. These metrics, along with associated loaded geometry, were evaluated at a common fixed pressure of 100 mmHg and group-specific estimated in vivo axial stretch values.

Bulk RNA-Seq

Total RNA was isolated from thoracic aortas as described for RT-PCR and quality control was assessed by nanodrop and an Agilent Bioanalyzer. Next-generation, whole-transcriptome sequencing was performed using a NovaSeq 6000 System (Illumina) at the Yale Center for Genome Analysis. RNA-seq reads were aligned to a reference genome (GRCm38) using short reads aligner STAR. Gene expression was quantified using RSEM with GENCODE annotation (mouse release M15, www.gencodegenes.org)[10,11]. Genes with 1 count per million in less than 10% of samples were removed. Read counts were normalized using the trimmed mean of M-values method (TMM) and differentially expressed genes were identified using edgeR (R package, using the exact test on the conditional distribution of counts)[12,13]. Differentially expressed genes between experimental groups with false discovery rate (FDR)-adjusted $P \leq 0.01$ were used for nGOseq functional enrichment.

Single-Cell RNA-Seq

Cells were isolated from the thoracic aorta as described for flow cytometry and incubated with cell-impermeant viability dye (Thermo Fisher) for 20 min at 4 °C. Viable, RFP^-/GFP^+ SMCs

were sorted with a FACSAria (BD Biosciences) and collected in 0.4% BSA/PBS. The selected cells were processed for single-cell RNA-seq library preparation using the Chromium™ Single Cell Platform (10x Genomics) as per the manufacturer's protocol. Briefly, single cells were partitioned into Gel Beads in Emulsion using the Chromium™ system (10x Genomics), followed by cell lysis and barcoded reverse transcription of RNA, cDNA amplification and shearing, and 5' adaptor and sample index attachment. The single-cell RNA-seq libraries were sequenced on a HiSeq 4000 System (Illumina) at the Yale Center for Genome Analysis.

For analyses of all transcripts (Supplemental Figures 10, Supplemental Figure 17, and Supplemental Table 7), the data from the barcoded library sequence was processed through Cell Ranger (10x Genomics) and this output was further processed in R using Seurat (Satija Lab). The reference mouse genome was customized by the addition of a reference genome sequence and gene annotation for the exogenous GFP gene. The data was filtered as follows: i) cells with less than 200 genes were eliminated and ii) cells with more than 10% mitochondrial gene expression were also eliminated, as these are generally believed to be apoptotic cells. This data was normalized in Seurat with default settings. Genes with the most variable expression were used for clustering by T-distributed Stochastic Neighbor Embedding (tSNE) and these projections were used for visualization.

For analyses of selected transcripts (Figure 6, Supplemental Figure 9, Supplemental Figure 11, Supplemental Figure 12, Supplemental Table 4, and Supplemental Table 6), we processed single-cell RNA-seq short reads from each cell group using UMI-tool[14]. Briefly, we first identified cell barcodes from R1 reads, extracted cell barcodes and UMIs from transcript sequences, and added these to the read names for R2 reads. We aligned R2 reads to the reference mouse genome build 38 (GRCm38) with short read aligner STAR[10,11]. The reference package was customized by the addition of a reference genome sequence and gene annotation for the exogenous GFP gene. Quantification was performed using UMI-tools count function to find the number of unique UMIs mapping to each gene (GENCODE mouse annotation, release M15). Raw count data was filtered by: i) requiring sample total read counts to be greater than 3,000 and the total number of detected genes per sample to be greater than 1,500, and ii) requiring that each gene was expressed in at least 5% of cells within each experimental group. In addition, we removed the Tsc1 read counts from the processed data matrix to prevent downstream analysis from segregating cells solely based on experimental genotype. Finalized read counts were normalized using TMM (edgeR R package) and used for downstream clustering and modeling[12,13], except that raw read counts were used for the analyses of hematopoietic lineage genes and co-expression studies to include absent leukocyte markers and low abundance transcription factors removed by the filter algorithm.

Deep learning framework

We built a custom deep learning methodology in TensorFlow to carry out unsupervised analysis and clustering of single-cell RNA-seq data using a *variational autoencoder* (*VAE*) framework[15-17].

Variational autoencoder

Briefly, suppose $\boldsymbol{x}$ is a vector of *D* variables, $\boldsymbol{z}$ is a vector of stochastic *latent* variables of dimension *M*, and $p_\theta(\boldsymbol{x}|\boldsymbol{z})$ is a parametric model of the joint distribution. When this model is parametrized by a neural network (discussed below), optimization becomes difficult due to the computational intractability of calculating the marginal likelihood. The most common method to avoid this is to apply *variational inference*, and optimize the estimated lower bound (ELBO):

$$\mathbb{E}_{x\sim q(\boldsymbol{x})}[\ln p(\boldsymbol{x})] \geq \mathbb{E}_{x\sim q(\boldsymbol{x})}\left[\mathbb{E}_{q_\varphi(\boldsymbol{z}|\boldsymbol{x})}[\ln p_\theta(\boldsymbol{x}|\boldsymbol{z}) + \ln p_\lambda(\boldsymbol{z})] - \ln q_\varphi(\boldsymbol{z}|\boldsymbol{x})\right]$$

where $q(\boldsymbol{x})$ is the empirical distribution, $q_\varphi(\boldsymbol{z}|\boldsymbol{x})$ is the *variational posterior* (i.e., *encoder*), $p_\theta(\boldsymbol{x}|\boldsymbol{z})$ is the *generative model* (i.e., the *decoder*), $p_\lambda(\boldsymbol{z})$ is the *prior*, and φ, θ, λ are their parameters. We re-formulated the *ELBO* function by assuming $\boldsymbol{z}$ is composed of continuous and independent

Gaussian distributions, using the *re-parameterization trick* for $q_\varphi(\boldsymbol{z}|\boldsymbol{x})$, and using a Monte Carlo estimate of the second expectation over *L* sample points:

$$\mathcal{L}(\varphi,\theta,\lambda) = \mathbb{E}_{x\sim q(x)}\left[\frac{1}{L}\sum_{l=1}^{L}\ln p_\theta(\boldsymbol{x}|\boldsymbol{z}_{\boldsymbol{\varphi}}^{(\boldsymbol{l})}) + \ln p_\lambda(\boldsymbol{z}_{\boldsymbol{\varphi}}^{(\boldsymbol{l})}) - \ln q_\varphi(\boldsymbol{z}_{\boldsymbol{\varphi}}^{(\boldsymbol{l})}|\boldsymbol{x})\right]$$

$$\boldsymbol{z}\sim\mathcal{N}(\mu,\Sigma)$$

$$\boldsymbol{z} = \mu + L\epsilon \;\; where \;\; \epsilon\sim\mathcal{N}(0,I) \;\; and \;\; \Sigma = LL^T$$

The first term is known as the *reconstruction error* and the second and third terms function similar to a *regularization term* that keeps the distributions of the *encoder* matching the *prior*. An alternative formulation is the *InfoVAE* prior, which instead uses the maximum mean discrepancy (*MMD*) and Gaussian kernels as the *regularization term*. *InfoVAE* maximizes the mutual information between ***x*** and ***z***, which can lead to a richer latent space[18].

$$\mathcal{L}(\varphi,\theta,\lambda) = \mathbb{E}_{x\sim q(x)}\left[\frac{1}{L}\sum_{l=1}^{L}\ln p_\theta\left(\boldsymbol{x}\middle|\boldsymbol{z}_{\boldsymbol{\varphi}}^{(\boldsymbol{l})}\right) - \beta * MMD(q_\varphi(\boldsymbol{z}_{\boldsymbol{\varphi}}^{(\boldsymbol{l})}|\boldsymbol{x})||\, p_\lambda(\boldsymbol{z}_{\boldsymbol{\varphi}}^{(\boldsymbol{l})}))\right]$$

$$MMD(p(\boldsymbol{z}))||q(\boldsymbol{z})) = \mathbb{E}_{p(z),p(z')}[k(z,z')] + \mathbb{E}_{q(z),q(z')}[k(z,z')] + \mathbb{E}_{p(z),q(z')}[k(z,z')]$$

$$k(z,z') = e^{\frac{\|z-z'\|^2}{2\sigma^2}}$$

$q_\varphi(\boldsymbol{z}|\boldsymbol{x})$, the *encoder*, is modeled using a typical feed-forward deep neural network structure, and similarly we let $p_\theta(\boldsymbol{x}|\boldsymbol{z})$, the *decoder*, be a zero-inflated negative binomial distribution with its parameters computed from ***z*** with a feed-forward deep neural network structure.

Zero-inflated negative binomial distribution (ZINB)

We model the posterior distribution of the *decoder* with a ZINB distribution in order to address the issue of *'dropout'*, where genes can be observed in one cell but not detected in another cell[18]. The probability mass function for the ZINB distribution (f_{ZINB}) is parameterized by inverse dispersion $\theta \geq 0$, mean $\mu \geq 0$, dropout probability $\pi \in [0,1]$, and Dirac function $\delta(\cdot)$[20,21].

$$f_{ZINB}(x,\mu,\theta,\pi) = \pi\delta(x) + (1-\pi)\left(\frac{(x+\theta)}{(\theta x+\theta)}\left(\frac{\theta}{\theta+\mu}\right)^{\theta}\left(\frac{\mu}{\theta+\mu}\right)^{x}\right)$$

The dropout probability π represents the likelihood of observing a zero in the data (i.e., observing *'dropout'*) instead of an actual numerical read count, thus inflating the observation of zeros within the distribution. We restrict the ZINB inverse dispersion parameter θ to be feature-dependent (i.e., the inverse dispersion is modeled across a gene and not on a per gene per sample basis) as it is both computationally easier and has shown to be sufficient for both single-cell RNA-seq and bulk RNA-seq analysis[20,22].

Feed-forward neural networks

The basic formulation of a simple fully-connected feed-forward frameworks where each layer (l) uses a specific activation function (ρ), is defined as:

$$f = \rho\left(\sum_{j=1}^{d}(W_j * X_j) + b_{d+1}\right)$$

Where the dimensions of *W* and *b* are determined by the number of neurons in each layer (d_1, d_2, … d_m). Each layer used *rectified linear units* (*ReLUs*) as activation functions:

$$\rho_l(z) = max(0,z)$$

In addition, we utilized the concept of *'dropout'* which randomly sets a portion of input values (η) to the layer to zero during the *training* phase[23]. This has a strong regularization effect, essentially by injecting random noise, that helps prevent models from over-fitting. Layers that included *'dropout'* were formulated as:

$$f = \rho\left(\sum_{j=1}^{d}\left(W_j * X_j\right) + b_{d+1}\right) * m_l \quad where \quad m_l \sim Bernoulli(\eta)$$

When evaluating models on *test* datasets the *'dropout'* mask is not used.

VAE model training

We used the *InfoVAE* formulation and the log-likelihood of the ZINB distribution as the three terms in the loss function. For learning, we utilized the *RMSProp* gradient descent algorithm with mini-batches size of 256. We trained models for a minimum of 250 epochs and utilized early stopping with a look ahead (i.e., patience) of 50 epochs (on a *validation* dataset consisting of a random 20% of the total data). In addition, the *regularization term* of the loss function was annealed (i.e., 'warmed-up') for the first 200 epochs of training. The per sample loss was weighted by the frequency of samples in the experimental design to help account for unbalanced datasets (i.e., total number of cells per experimental condition). The final log-likelihoods were generated by bootstrap sampling 100 times from the final model and calculating the mean value.

VAE hyper-parameter search

The following hyper-parameters were optimized using a random search strategy over the parameter grid: layer-dimension, number of layers, dropout-rate, learning rate, and latent-dimension. We selected the model with the lowest *validation loss*.

PhenoGraph clustering

We fixed the hyper-parameters and structure of the zero-inflated VAE and ran 100 replicate model runs. We applied the *PhenoGraph* algorithm, using *k = 30* nearest-neighbors and the Jaccard similarity metric, to cluster the *latent* space of each run[24,25]. We determined the number of clusters within the dataset by selecting the most frequent across the 100 runs (in case of ties we selected the lower cluster number). Lastly, we calculated a consensus clustering across all 100 runs using the using the *Cluster-based Similarity Partitioning Algorithm*, spectral-clustering, and the specified cluster number (as determined above)[26,27].

Stitch networks – encoder + deep artificial neural network classification layer

A traditional deep artificial neural network, consisting of 3 layers with 32 hidden nodes, *ReLU* activation functions, and dropout, was appended to the *encoder* network. This allowed us to evaluate classification performance using the *latent* space and the consensus clustering labels. The final layer used a *softmax* function, with the number of neurons equal to the number of clusters (*K*), to convert the logits to probabilities:

$$\varphi(f_m)_j = \frac{e^{\boldsymbol{x}_j}}{\sum_{k=1}^{K} e^{\boldsymbol{x}_k}} \; for \; j = 1, \ldots, K$$

We used the categorical cross-entropy loss function, where B_n is the mini-batch size, t_i is the correct class index, and p_i is the class probability from the softmax layer:

$$L_T = \sum_{i=1}^{B_n} t_i \log(p_i)$$

The full dataset was split into 80% *training* and 20% *test* datasets (stratified by cluster labels). For learning, we utilized the *RMSProp* gradient descent algorithm with mini-batches size

of 256. We trained models for a minimum of 250 epochs and utilized early stopping with a look ahead of 50 epochs (on a *validation* dataset consisting of a random 20% of the *training* data). We utilized the optimal hyper-parameters for learning rate and dropout from the VAE model, as we found these had minimal effects on classification performance. With the fixed the hyper-parameters, network-structure, and consensus cluster labels, we ran a final 100 replicate model runs. Models were evaluated using the held-out *test* dataset with the following metrics: i) AUC, ii) F1-scores, iii) overall accuracy, iv) balanced accuracy, v) sensitivity, and vi) specificity.

Sensitivity mapping of stitch networks

Sensitivity mapping was originally developed for visualizing the sensitivities of image classification to input pixels from deep neural networks[28]. It is a gradient-based local sensitivity analysis technique that evaluates the relative importance of input variables with respect to output classes. Given an input sample *x*, the final layer of a neural network is traditionally a class activation function F_K, which gives an associated score to each of the *K* classes. The final class is determined by taking the maximum of the class activation function. A very simplistic way of estimating the *importance* of each feature in a sample, known as the sensitivity map, G_k, is to differentiate the class activation function with respect to the input sample *x*:

$$G_k = \frac{\partial F_k(x)}{\partial x}$$

Therefore, G_k indicates how sensitive the class activation function, for a specific class *k*, is to perturbations in the features of sample *x* and thus gives a metric of feature *importance*. This has shown to be a useful strategy for attempting to 'deconstruct' the black box of deep learning techniques[28]. Herein, we use an extension to this simple 'raw gradient' approach, known as *SmoothGrad*, which sharpens sensitivity maps by injecting noise to remove noise[28]. *SmoothGrad* takes random samples within the neighborhood of *x*, by injecting Gaussian noise with standard deviation σ, and averages the resulting sensitivity maps. The two *SmoothGrad* hyper-parameters σ and n were set to 15% of min/max and 25 respectively as recommended[28].

$$\widehat{G_k} = \frac{1}{n}\sum_{1}^{n} G_k\left(x + \mathcal{N}(0, \sigma^2)\right)$$

Contrary to image analysis, where each image is unique in the location, shape, morphology, etc of the object to classify, there is no spatial information/diversity encoded in genomic datasets. Thus, an individual feature measurement at a position in the input data (e.g. feature *d* across *n* samples, $x_{1,d}, \ldots, x_{n,d}$) is always the same feature (representing the same genomic measurement). Therefore, we aggregated *SmoothGrad* sensitivity maps, calculated using only the *training* dataset, across all samples of a specific predicted class *k* using the mean statistic. We then calculated the mean of the sensitivity maps across the final 100 replicate model runs in order to smooth fluctuations in feature *importance* across multiple runs. Lastly, the per class sensitivity maps are partially dependent upon each other due to the multinomial nature of the classification model (i.e., if class A is sensitive to feature *d* class B and class C are also sensitive to feature *d* as the presence/lack of feature d rules out/in class A), thus we used the minimum rank of across all class sensitivity maps as the final feature *importance* rankings.

Nested GOSeq (nGOseq) Functional Enrichment

nGOseq analysis was performed on both bulk and single-cell RNA-seq datasets: i) bulk RNA-seq – differentially expressed genes with false discovery rate corrected *P* values ≤ 0.01 and ii) single-cell RNA-seq – the top 10% most informative genes from sensitivity mapping. Both analyses used all possible annotated genes as the background distributions. Briefly, GOseq analysis was performed to identify enriched gene ontology (GO) terms[29]. Nested GOseq (nGOseq), a modified version of the nested Expression Analysis Systematic Explorer (nEASE)

algorithm, was then used to identify enriched nested GO (nGO) terms driving the statistical enrichment of upper-level GOseq terms[30,31].

Supplemental Methods References

1. Kozel BA, Wachi H, Davis EC, Mecham RP. Domains in tropoelastin that mediate elastin deposition in vitro and in vivo. *J Biol Chem*. 2003;278(20):18491-18498.
2. Weinbaum JS, Broekelmann TJ, Pierce RA, Werneck CC, Segade F, Craft CS, Knutsen RH, Mecham RP. Deficiency in microfibril-associated glycoprotein-1 leads to complex phenotypes in multiple organ systems. *J Biol Chem*. 2008;283(37):25533-25543.
3. Gleason RL, Gray SP, Wilson E, Humphrey JD. A multiaxial computer-controlled organ culture and biomechanical device for mouse carotid arteries. *J Biomech Eng*. 2004;126(6):787-795.
4. Bersi MR, Khosravi R, Wujciak AJ, Harrison DG, Humphrey JD. Differential cell-matrix mechanoadaptations and inflammation drive regional propensities to aortic fibrosis, aneurysm or dissection in hypertension. *J R Soc Interface*. 2017;14(136):20170327.
5. Ferruzzi J, Bersi MR, Uman S, Yanagisawa H, Humphrey JD. Decreased elastic energy storage, not increased material stiffness, characterizes central artery dysfunction in fibulin-5 deficiency independent of sex. *J Biomech Eng*. 2015;137(3):031007.
6. Bellini C, et al. Comparison of 10 murine models reveals a distinct biomechanical phenotype in thoracic aortic aneurysms. *J R Soc Interface*. 2017;14(130):20161036.
7. Bellini C, Caulk AW, Li G, Tellides G, Humphrey JD. Biomechanical Phenotyping of the Murine Aorta: What Is the Best Control? *J Biomech Eng*. 2017;139(4):044501.
8. Ferruzzi J, Collins MJ, Yeh AT, Humphrey JD. Mechanical assessment of elastin integrity in fibrillin-1-deficient carotid arteries: implications for Marfan syndrome. *Cardiovasc Res*. 2011;92(2):287-295.
9. Baek S, Gleason RL, Rajagopal KR, Humphrey JD. Theory of small on large: Potential utility in computations of fluid–solid interactions in arteries. *Comput Methods Appl Mech Eng*. 2007;196(31):3070-3078.
10. Dobin A, et al. STAR: ultrafast universal RNA-seq aligner. *Bioinformatics*. 2013;29(1):15-21.
11. Li B, Dewey CN. RSEM: accurate transcript quantification from RNA-Seq data with or without a reference genome. *BMC Bioinformatics*. 2011;12:323.
12. Robinson MD, Oshlack A. A scaling normalization method for differential expression analysis of RNA-seq data. *Genome Biol*. 2010;11(3):R25.
13. Robinson MD, McCarthy DJ, Smyth GK. edgeR: a Bioconductor package for differential expression analysis of digital gene expression data. *Bioinformatics*. 2010;26(1):139-140.
14. Smith T, Heger A, Sudbery I. UMI-tools: modeling sequencing errors in Unique Molecular Identifiers to improve quantification accuracy. *Genome Res*. 2017;27(3):491-499.
15. Tomczak JM, Welling M. VAE with a VampPrior. 2017. arXiv:1705.07120.
16. Doersch C. Tutorial on Variational Autoencoders. 2016. arXiv:1606.05908.
17. Abadi M, et al. TensorFlow: Large-scale machine learning on heterogeneous distributed systems. 2016. arXiv:1603.04467.
18. Zhao S, Song J, Ermon S. InfoVAE: informational maximizing variational autoencoders. 2017. arXiv:1706.02262.
19. Kharchenko PV, Silberstein L, Scadden DT. Bayesian approach to single-cell differential expression analysis. *Nat Methods*. 2014;11(7):740-742.
20. Risso D, Perraudeau F, Gribkova S, Dudoit S, Vert JP. A general and flexible method for signal extraction from single-cell RNA-seq data. Nat Commun. 2018;9(1):284.
21. Lopez R, Regier J, Cole M, Jordan M, Yosef N. A deep generative model for gene expression profiles from single-cell RNA sequencing. 2017. arXiv:1709.02082.
22. Robinson MD, Smyth GK. Small-sample estimation of negative binomial dispersion, with applications to SAGE data. *Biostatistics*. 2008;9(2):321-332.
23. Srivastava N, Hinton G, Krizhevsky A, Sutskever I, Salakhutdinov R. Dropout: A simple way to prevent neural networks from overfitting. *J Mach Learn Res*. 2014;15:1929-1958.

24. Levine JH, et al. Data-Driven Phenotypic Dissection of AML Reveals Progenitor-like Cells that Correlate with Prognosis. *Cell*. 2015;162(1):184-197.
25. Shekhar K, et al. Comprehensive Classification of Retinal Bipolar Neurons by Single-Cell Transcriptomics. *Cell*. 2016;166(5):1308-1323.
26. Strehl A, Ghosh J. Cluster ensembles – A knowledge reuse framework for combining multiple partitions. *J Mach Learn Res*. 2002;3(Dec):583-617.
27. Shi J, Malik J. Normalized cuts and image segmentation. *IEEE Trans Pattern Anal Mach Intell*. 2000;22(8):888-905.
28. Smilkov D, Thorat N, Kim B, Viegas F, Wattenberg M. SmoothGrad: removing noise by adding noise. 2017. arXiv:1706.03825.
29. Young MD, Wakefield MJ, Smyth GK, Oshlack A. Gene ontology analysis for RNA-seq: accounting for selection bias. *Genome Biol*. 2010;11(2):R14.
30. Chittenden TW, et al. nEASE: a method for gene ontology subclassification of high-throughput gene expression data. *Bioinformatics*. 2012;28(5):726-728.
31. Yu P, et al. FGF-dependent metabolic control of vascular development. *Nature*. 2017;545(7653):224-228.

Supplemental Figures

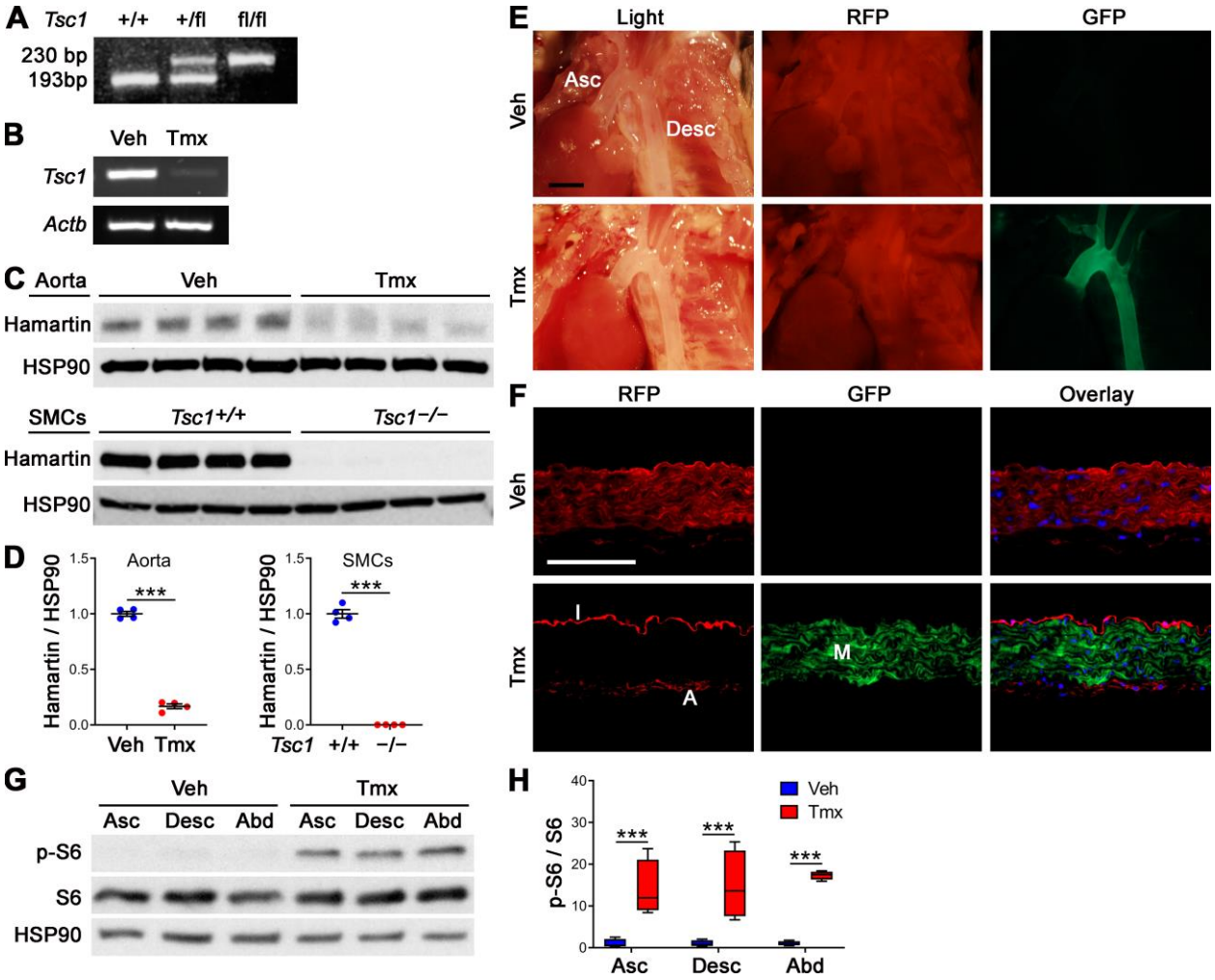

Supplemental Figure 1: Conditional deletion of *Tsc1* in SMCs. *Tsc1*$^{fl/fl}$*.Myh11-CreER*^{T2}*.mT/mG* mice were treated with vehicle (Veh) or tamoxifen (Tmx) at 1.5 wk of age and their thoracic aortas were analyzed at 12 wk. For isolation of GFP^{+} SMCs, *Myh11-CreER*^{T2}*.mT/mG* mice lacking *Tsc1*$^{fl/fl}$ (*Tsc1*$^{+/+}$) and *Tsc1*$^{fl/fl}$*.Myh11-CreER*^{T2}*.mT/mG* mice (*Tsc1*$^{-/-}$) were treated with tamoxifen at 1.5 wk. (**A**) PCR for 193 bp wild-type and 230 bp floxed *Tsc1* DNA. (**B**) PCR for *Tsc1* exon 17 and *Actb* mRNA. (**C**) Western blots for hamartin and HSP90 in thoracic aortas or isolated GFP^{+} aortic SMCs and (**D**) densitometry of hamartin relative to HSP90 (n = 4). (**E**) Light and fluorescence microscopy for RFP and GFP expression of ascending (Asc) and descending (Desc) aortas in situ (bar = 2 mm). (**F**) Fluorescence microscopy of ascending aorta transverse sections showing tamoxifen-dependent loss of RFP (red) and induction of GFP (green) expression by vessel wall cells selectively within the media (M), but not the intima (I) or adventitia (A), with DAPI-labeled nuclei (blue) in overlays (bar = 100 µm). (**G**) Western blots for phospho-S6, S6, and HSP90 in ascending, descending, and abdominal (Abd) segments of the aorta and (**H**) densitometry of p-S6 relative to S6 (n = 4). Data are represented as individual values with mean ± SEM bars or as box-and-whisker plots with interquartile range, median, minimum, and maximum; ***P < 0.001 for Tmx vs. Veh, t-test (panel D) or 2-way ANOVA (panel H).

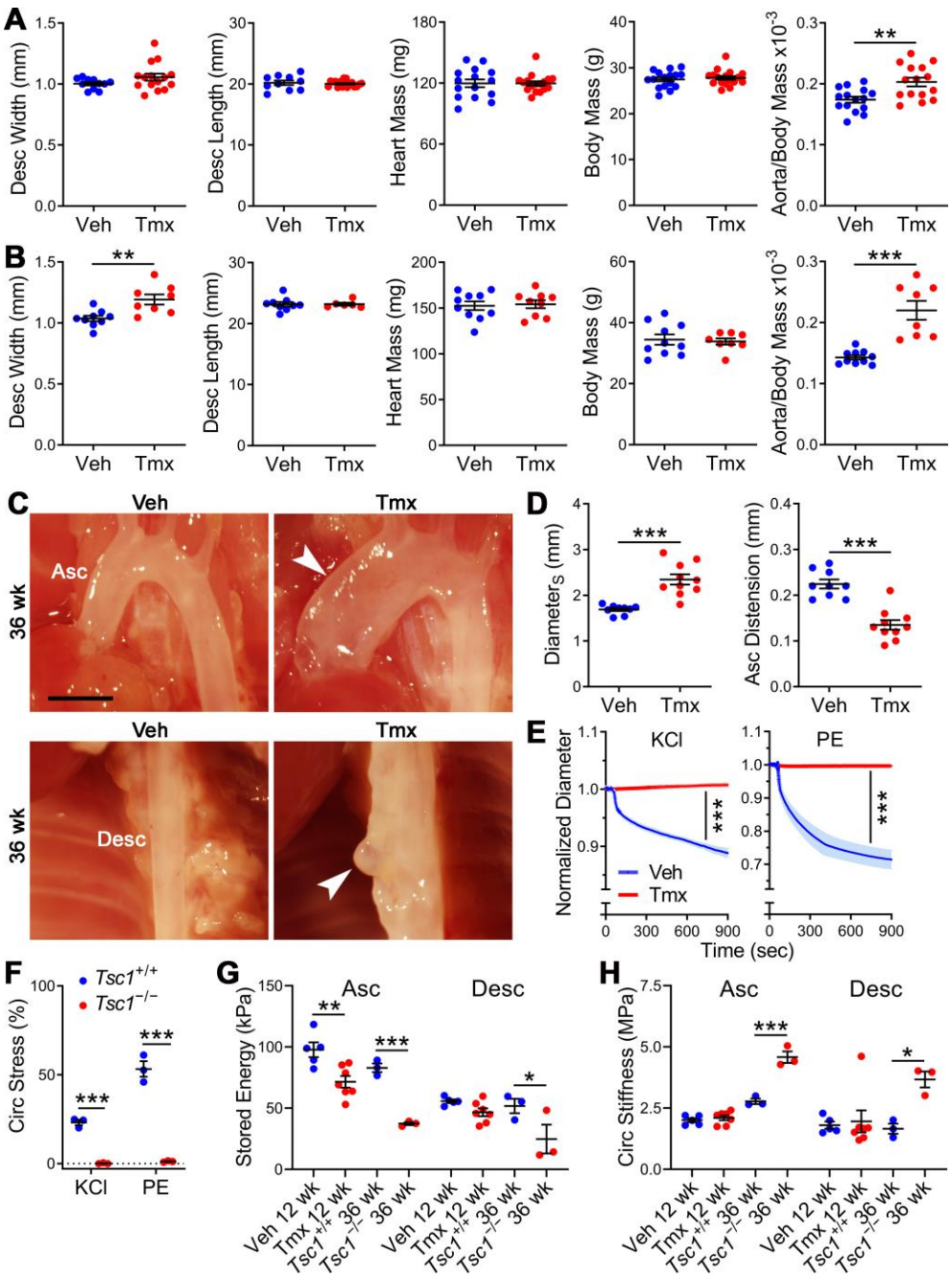

Supplemental Figure 2: *Tsc1* deletion in SMCs leads to progressive aortic disease and dysfunction. *Tsc1*$^{fl/fl}$*.Myh11-CreER*^{T2}*.mT/mG* mice were treated with tamoxifen (Tmx) or vehicle (Veh) at 1.5 wk of age and their aortas were serially examined. (**A**) In situ width and length of unpressurized descending (Desc) thoracic segments, heart and body mass, and indexed thoracic aorta to body mass at 12 wk (*n* = 10-17). (**B**) Similar analyses at 36 wk (*n* = 6-10). (**C**) In situ examination of ascending (Asc) and descending (Desc) thoracic aortas showing advanced aneurysms (white arrows) at 36 wk (bar = 2 mm). (**D**) In vivo ascending aorta systolic (s) diameter and distension at 36 wk (*n* = 9-10). For biomechanical analyses at 36 wk, *Tsc1*$^{fl/fl}$*.Myh11-CreER*^{T2}*.mT/mG* and *Myh11-CreER*^{T2}*.mT/mG* mice were treated with tamoxifen at 1.5 wk of age and are denoted as *Tsc1*$^{-/-}$ and *Tsc1*$^{+/+}$, respectively. (**E**) Ex vivo ascending aorta outer diameter, normalized to pretreatment value, in response to 100 mM KCl or 1 μM phenylephrine (PE) and (**F**) the associated reduction in circumferential (Circ) stress at 36 wk (*n* = 3). Structural responses of ascending and descending thoracic aorta segments at 12 and 36 wk as revealed by comparisons of (**G**) elastically stored energy at a fixed pressure of 100 mmHg and (**H**) circumferential material stiffness (*n* = 3-7). Data are represented as individual values with mean ± SEM bars or as line plots of mean ± SEM; **P* < 0.05, ***P* < 0.01, ****P* < 0.001, t-test (panels A, B, D), 2-way repeated measures ANOVA (panel E), or 2-way ANOVA (panels F, G, H).

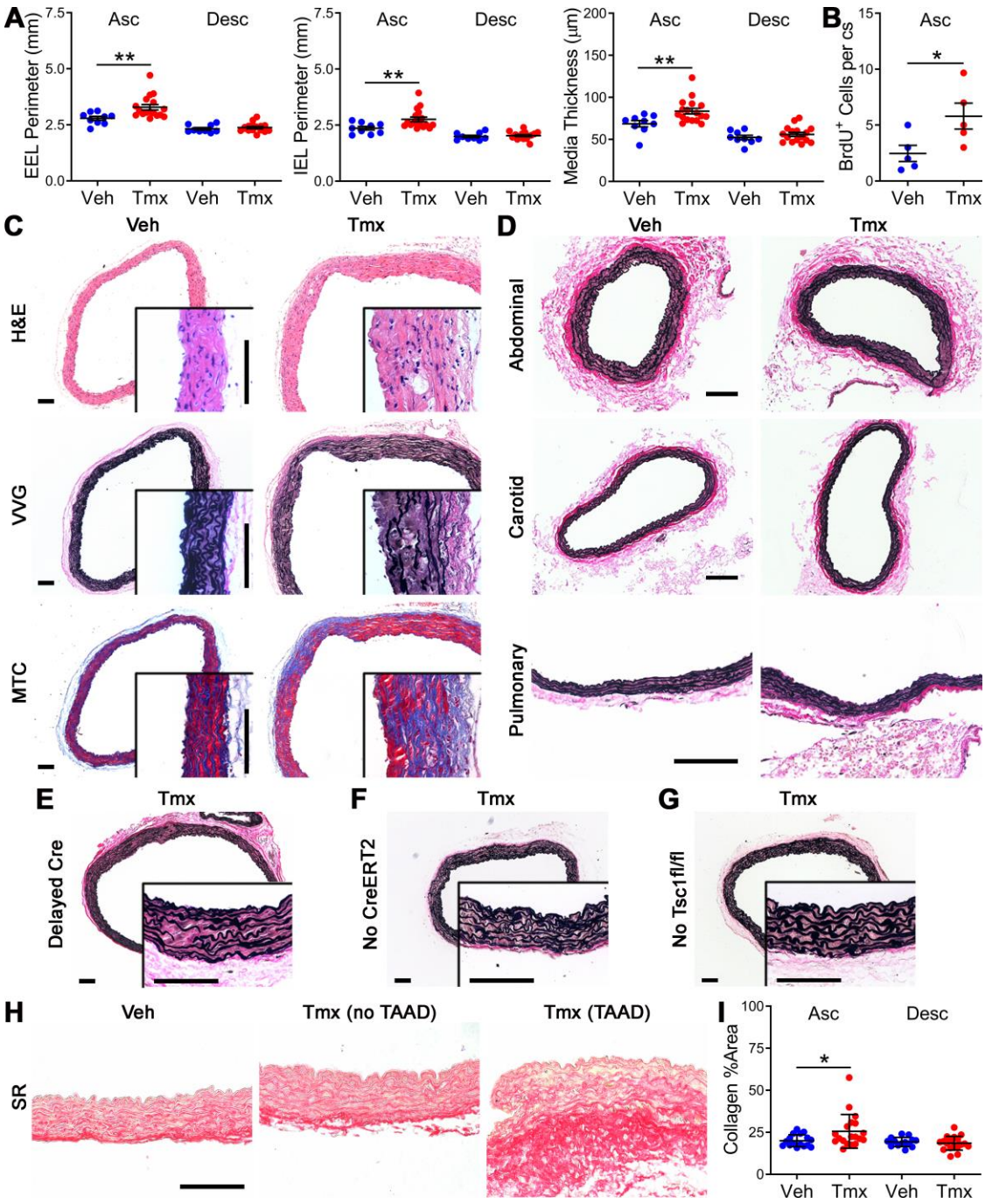

Supplemental Figure 3: Spectrum of aortic pathology. Mice were treated with tamoxifen (Tmx) or vehicle (Veh) at different times and various arteries were analyzed by histology. (**A**) Increased external elastic lamina (EEL) perimeter, internal elastic lamina (IEL) perimeter, and medial thickness of ascending (Asc) but not descending (Desc) thoracic aorta from *Tsc1$^{fl/fl}$.Myh11-CreER^{T2}.mT/mG* mice induced at 1.5 wk and analyzed at 12 wk (n = 9-17). (**B**) Increased number of BrdU^{+} medial cells per cross-section (cs) in ascending aortas of these animals at 5 wk (n = 5). (**C**) Severe medial degeneration of ascending aortas from *Tsc1$^{fl/fl}$.Myh11-CreER^{T2}.mT/mG* mice induced at 1.5 wk and analyzed at 36 wk by H&E, Verhoeff-Van Gieson (VVG), and Masson's trichrome (MTC) stains (bars = 100 μm). (**D**) Mild dilatation and few elastin breaks of abdominal aorta, carotid artery, and pulmonary artery from *Tsc1$^{fl/fl}$.Myh11-CreER^{T2}.mT/mG* mice induced at 1.5 wk and analyzed at 24 wk (bars = 100 μm). Histology of ascending aortas from (**E**) *Tsc1$^{fl/fl}$.Myh11-CreER^{T2}.mT/mG* mice induced in delayed fashion at 12 wk and analyzed at 24 wk showing mild medial degeneration, (**F**) *Tsc1$^{fl/fl}$.mT/mG* mice induced at 1.5 wk and analyzed at 12 wk showing normal media, as well as (**G**) *Myh11-CreER^{T2}.mT/mG* mice induced at 1.5 wk and analyzed at 12 wk showing normal media (bars = 100 μm). (**H**) Sirius red (SR) stains of ascending aortas without or with TAAD from *Tsc1$^{fl/fl}$.Myh11-CreER^{T2}.mT/mG* mice induced at 1.5 wk and analyzed at 12 wk (bar = 100 μm) and (**I**) collagen fraction of media (n = 14-19). Data are represented as individual values with mean ± SEM bars; **P* < 0.05, ***P* < 0.01 for Tmx vs. Veh, 2-way ANOVA (panels A, I) or t-test (panel B).

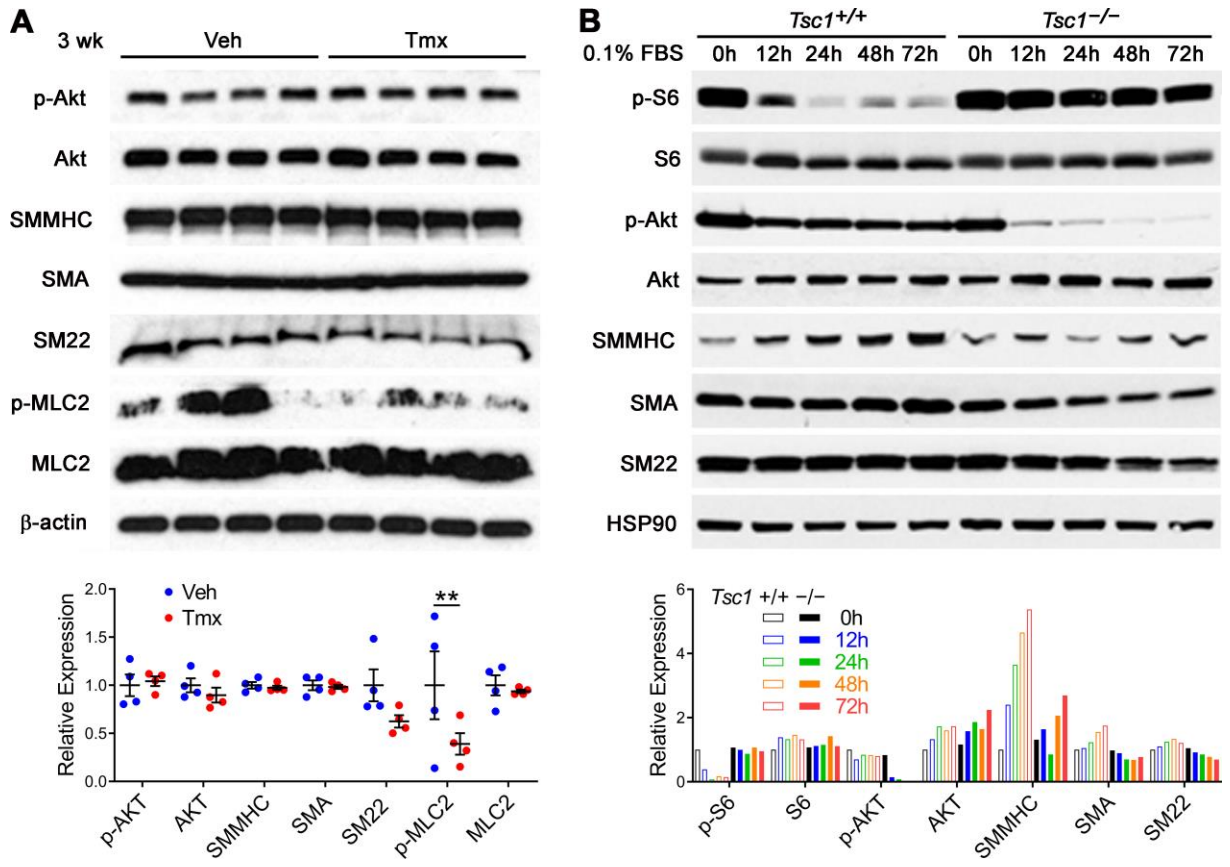

Supplemental Figure 4: mTOR activation and SMC contractile phenotype. (**A**) *Tsc1$^{fl/fl}$.Myh11-CreER^{T2}.mT/mG* mice were treated with tamoxifen (Tmx) or vehicle (Veh) at 1.5 wk of age and the thoracic aortas were analyzed by western blot at 3 wk for the indicated proteins with band densities normalized to loading controls and means (n = 4). Data are represented as individual values with mean ± SEM bars; **P < 0.01, 1-way ANOVA. (**B**) FACS-sorted, GFP$^+$ SMCs were cultured from enzymatically digested thoracic aortas of Cre-induced *Tsc1$^{fl/fl}$.Myh11-CreER^{T2}.mT/mG* (denoted as *Tsc1$^{-/-}$*) and *Myh11-CreER^{T2}.mT/mG* (denoted as *Tsc1$^{+/+}$*) mice and analyzed by western blot after serum withdrawal from 10% to 0.1% FBS for 0-72 h. Data are represented as individual values over time.

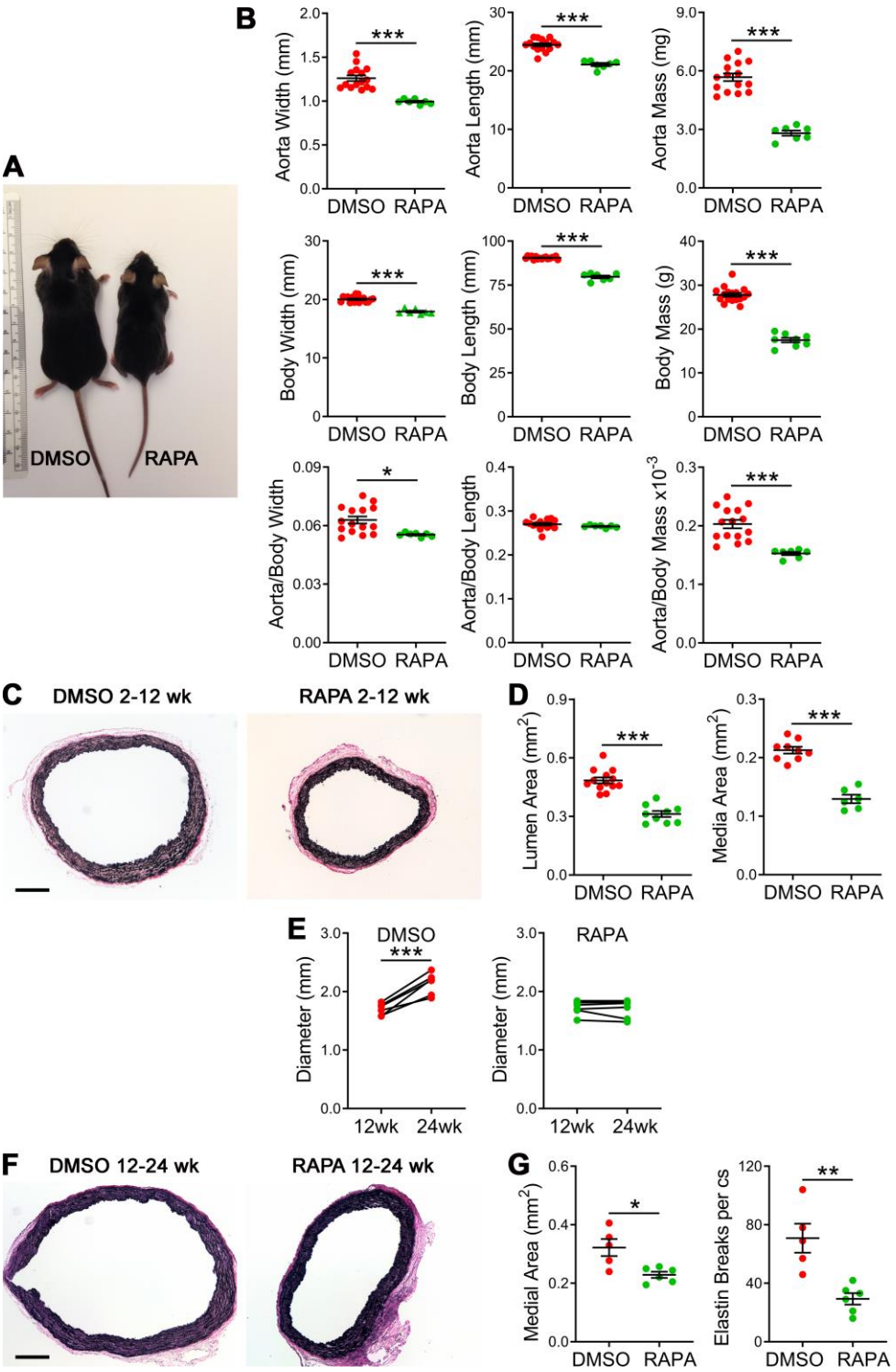

Supplemental Figure 5: mTOR inhibition prevents TAAD. *Tsc1$^{fl/fl}$.Myh11-CreER^{T2}.mT/mG* mice were induced with tamoxifen at 1.5 wk of age and then treated with 1% DMSO or rapamycin (RAPA) at 2 mg/kg/d i.p. from 2 to 12 wk (i.e. before disease initiation). mTOR inhibition resulted in (**A**) stunted growth, (**B**) decreased ascending aorta width, thoracic aorta length, and thoracic aorta mass indexed to body width, length, and mass, and (**C**) smaller ascending aortas by histology (bar = 200 μm) with (**D**) decreased lumen and media areas (n = 7-17, results from DMSO-treated mice were pooled with similar results from untreated mice for greater statistical power). Additionally, treatment with rapamycin at 2 mg/kg/d i.p. from 12 to 24 wk (i.e. after disease initiation) prevented (**E**) expansion of end-systolic diameter by serial ultrasound and (**F**) TAAD progression (bar = 200 μm) with (**G**) decreased medial area and fewer elastin breaks per cross-section (cs) of ascending aortas, (n = 5-6). Data are represented as individual values with mean ± SEM bars or with connecting lines; *P < 0.05, **P < 0.01, ***P < 0.001, t-test (panels B, D, G) or paired t-test (panel E).

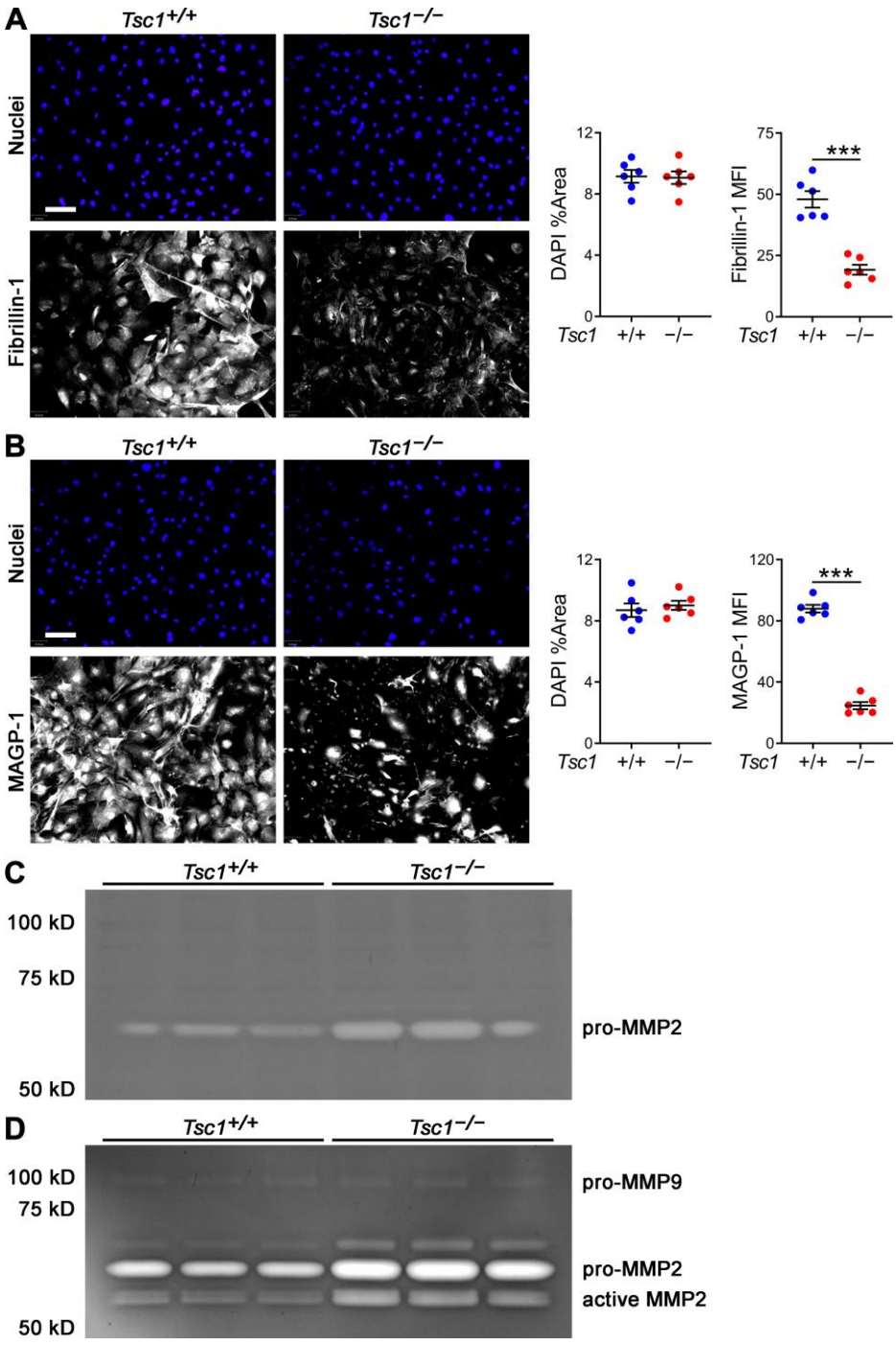

Supplemental Figure 6: Decreased ECM production and increased ECM degradation by mTOR-activated SMCs. *Myh11-CreER^{T2}.mT/mG* (*Tsc1$^{+/+}$*) and *Tsc1$^{fl/fl}$.Myh11-CreER^{T2}.mT/mG* (*Tsc1$^{-/-}$*) mice were treated with tamoxifen at 1.5 wk of age and SMCs were isolated from thoracic aortas based on GFP expression. (**A**) Fibrillin-1 and (**B**) MAGP-1 immunostaining (white) with DAPI labelling of nuclei (blue) in SMC cultures from 3 wk-old mice (bars = 100 µm); protein expression quantified as mean fluorescence intensity (MFI) and nuclei quantified as %Area ($n = 6$). Data are represented as individual values with mean ± SEM bars; ***$P < 0.001$ for *Tsc1$^{-/-}$* vs. *Tsc1$^{+/+}$*, t-test. Zymography for gelatinase activity in (**C**) cell lysates and (**D**) culture supernatant of cultured SMCs from 24 wk-old mice with pro- and active MMP bands labeled.

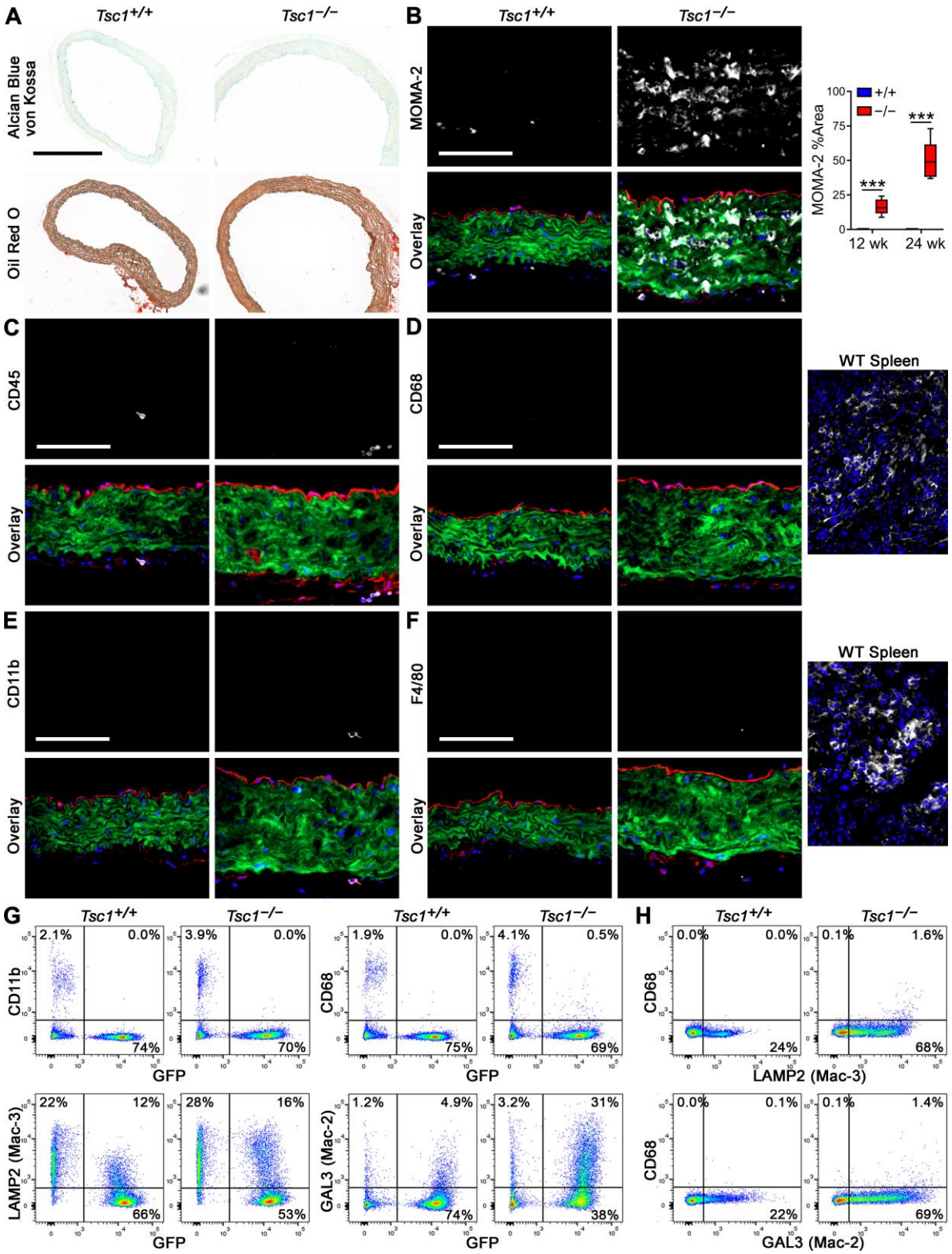

Supplemental Figure 7: Medial SMCs acquire limited macrophage markers. *Myh11-CreER^{T2}.mT/mG* (*Tsc1$^{+/+}$*) and *Tsc1$^{fl/fl}$.Myh11-CreER^{T2}.mT/mG* (*Tsc1$^{-/-}$*) mice were treated with tamoxifen at 1.5 wk and the thoracic aortas were analyzed at 24 wk. (**A**) Histological stains for glycosaminoglycans, mineralization, and lipids (bar = 500 μm). Immunofluorescence microscopy for (**B**) MOMA-2, (**C**) CD45, (**D**) CD68, (**E**) CD11b, and (**F**) F4/80 (white) with RFP, GFP, and DAPI overlay (bars = 100 μm); control staining in spleen and quantification of MOMA2 staining (n = 8). Data are represented as box-and-whisker plots with interquartile range, median, minimum, and maximum; *** $P < 0.001$, 2-way ANOVA. Flow cytometry for expression of (**G**) macrophage markers in both GFP$^-$ and GFP$^+$ cells and (**H**) CD68 by LAMP2 (Mac-3) and GAL3 (Mac-2) expressing GFP$^+$ SMCs.

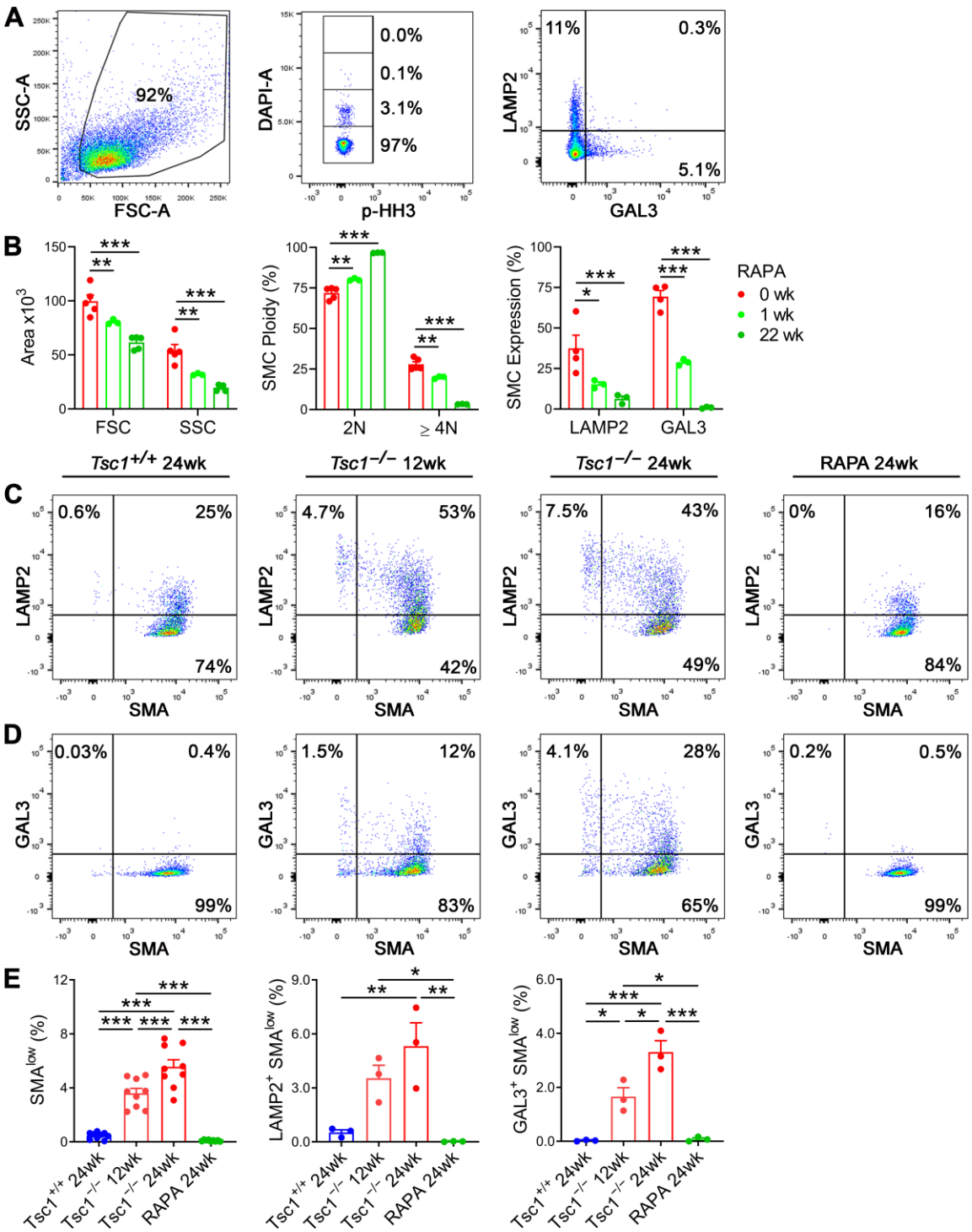

Supplemental Figure 8: Rapamycin prevents phenotypic modulation of SMCs. *Myh11-CreER^{T2}.mT/mG* (*Tsc1$^{+/+}$*) and *Tsc1$^{fl/fl}$.Myh11-CreER^{T2}.mT/mG* (*Tsc1$^{-/-}$*) mice were treated with tamoxifen at 1.5 wk. *Tsc1$^{-/-}$* animals were either untreated (0 wk) or treated with rapamycin (RAPA) at 2 mg/kg/d i.p. long-term (22 wk duration) from 2 to 24 wk of age or short-term (1 wk duration) from 23 to 24 wk of age. (**A**) Size, ploidy, and LAMP2/GAL3 expression of GFP$^+$ SMCs isolated from thoracic aortas of 24 wk-old *Tsc1$^{-/-}$* mice treated long-term with rapamycin (refer to Figure 5 for characteristics of cells not treated with rapamycin) and (**B**) comparisons among GFP$^+$ SMCs isolated from thoracic aortas of 24 wk-old *Tsc1$^{-/-}$* mice either untreated or treated short-term or long-term with rapamycin (n = 3-5). (**C**, **D**) Representative flow cytometry analyses of LAMP2 and GAL3 versus SMA expression by GFP$^+$ SMCs isolated from thoracic aortas of 24 wk-old *Tsc1$^{+/+}$* mice, 12 and 24 wk-old *Tsc1$^{-/-}$* mice not treated with rapamycin, and 24 wk-old *Tsc1$^{-/-}$* mice treated long-term with rapamycin from 2 to 24 wk of age and (**E**) comparisons of SMA^{low} cells (n = 9), LAMP2$^+$ SMA^{low} cells (n = 3), and GAL3$^+$ SMA^{low} cells (n = 3). Data are represented as individual values with mean ± SEM bars; *P < 0.05, **P < 0.01, ***P < 0.001, 2-way ANOVA (panel B) and 1-way ANOVA (panel E).

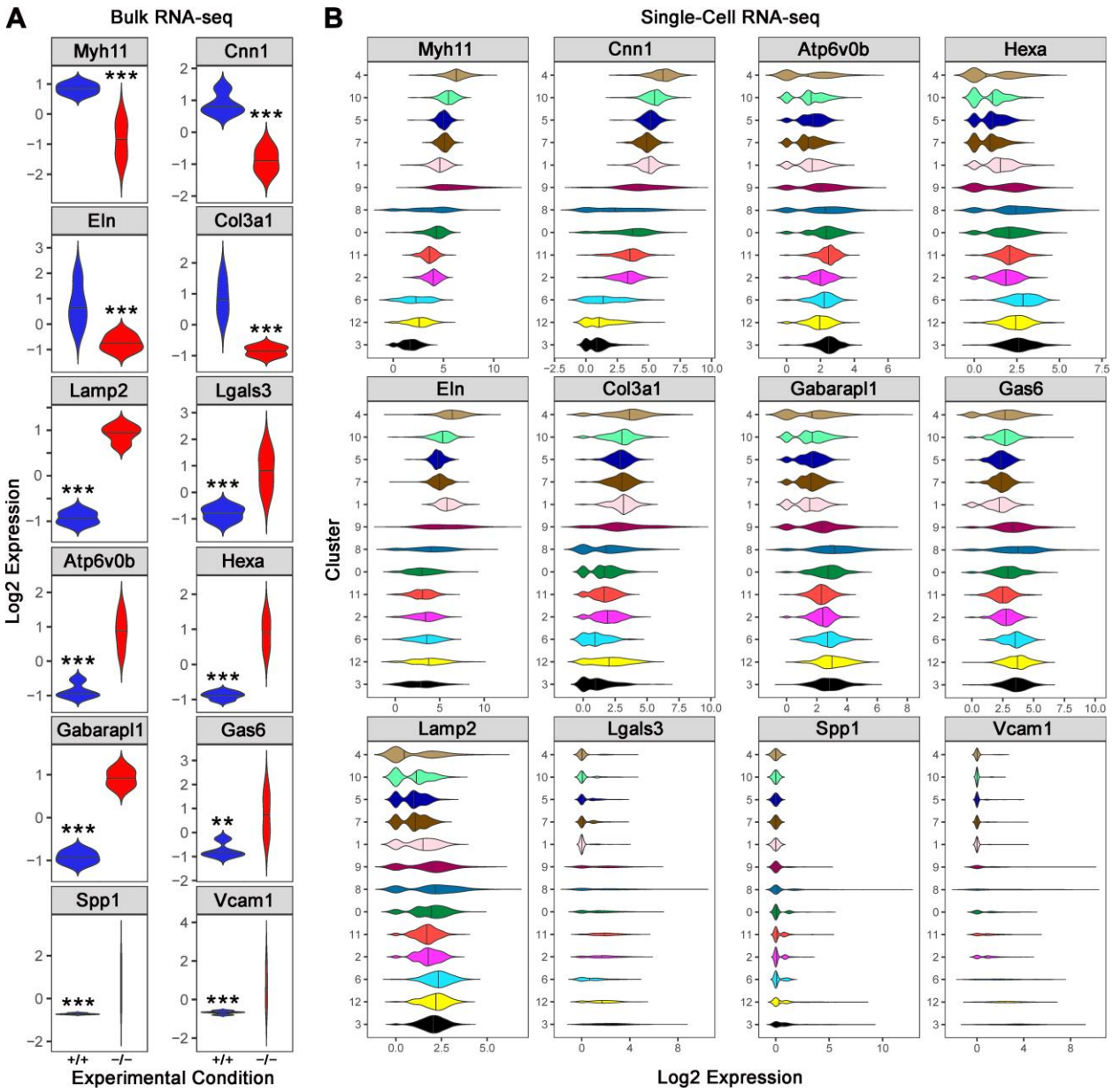

Supplemental Figure 9: Decreased contractile and synthetic markers and increased markers of degradative organelles and cellular activation in SMCs. *Myh11-CreER^{T2}.mT/mG* (*Tsc1$^{+/+}$*) and *Tsc1$^{fl/fl}$.Myh11-CreER^{T2}.mT/mG* (*Tsc1$^{-/-}$*) mice were treated with tamoxifen at 1.5 wk and the thoracic aortas and isolated GFP^{+} SMCs were analyzed at 24 wk. Violin plots representing RNA expression for selected genes (2 from each phenotype group shown in Figure 6) from (**A**) bulk RNA-seq of thoracic aortas and (**B**) single-cell RNA-seq of fate-mapped SMCs; FDR-adjusted *P* values, ***P* < 0.01, ****P* < 0.001.

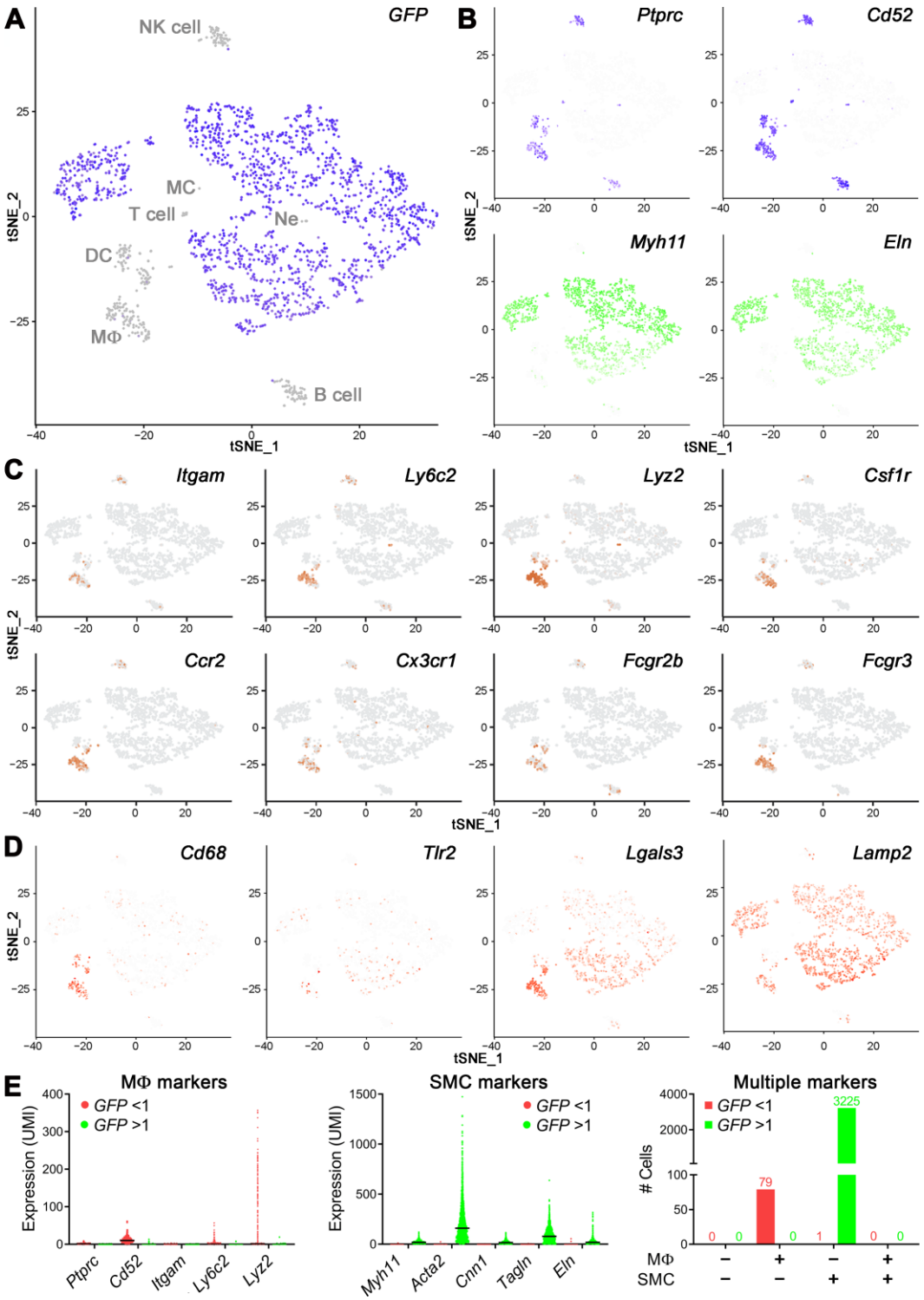

Supplemental Figure 10: Expression of macrophage and SMC markers. Single-cell RNA-seq of thoracic aortas of 24 wk-old, tamoxifen-treated *Myh11-CreER^{T2}.mT/mG* (*Tsc1$^{+/+}$*) and *Tsc1$^{fl/fl}$.Myh11-CreER^{T2}.mT/mG* (*Tsc1$^{-/-}$*) mice revealed absent *GFP* expression by 15.8% *Tsc1$^{+/+}$* and 0.6% *Tsc1$^{-/-}$* cells allowing for additional comparisons of SMCs to contaminating cells. (**A**) *GFP^{-}* cells (grey color) were identified as subtypes of leukocytes based on multiple lineage markers (MΦ: macrophage, DC: dendritic cell, Ne: neutrophil, MC: mast cell, NK: natural killer) and (**B**) expressed pan-leukocyte markers (*Ptprc* encoding CD45 and *Cd52*) but not SMC markers (*Myh11* and *Eln*). (**C**) *GFP^{+}* SMCs did not express myeloid lineage markers (*Itgam* encoding CD11b, *Ly6c2*, *Lyz2*, *Csf1r*, *Ccr2*, *Cx3cr1*, *Fcgr2b*, and *Fcgr3*) except for (**D**) weak or moderate expression of limited macrophage-associated molecules (*Cd68*, *Tlr2*, *Lgals3*, and *Lamp2*). (**E**) Expression of selected macrophage and SMC markers by *GFP^{-}* and *GFP^{+}* cells and the number of cells expressing 3 macrophage genes (*Cd52*, *Ly6c2*, and *Lyz2* all > 1) and/or 3 SMC genes (*Myh11*, *Acta2*, and *Cnn1* all > 1). Data are represented as individual values with median or as column bars of cell numbers.

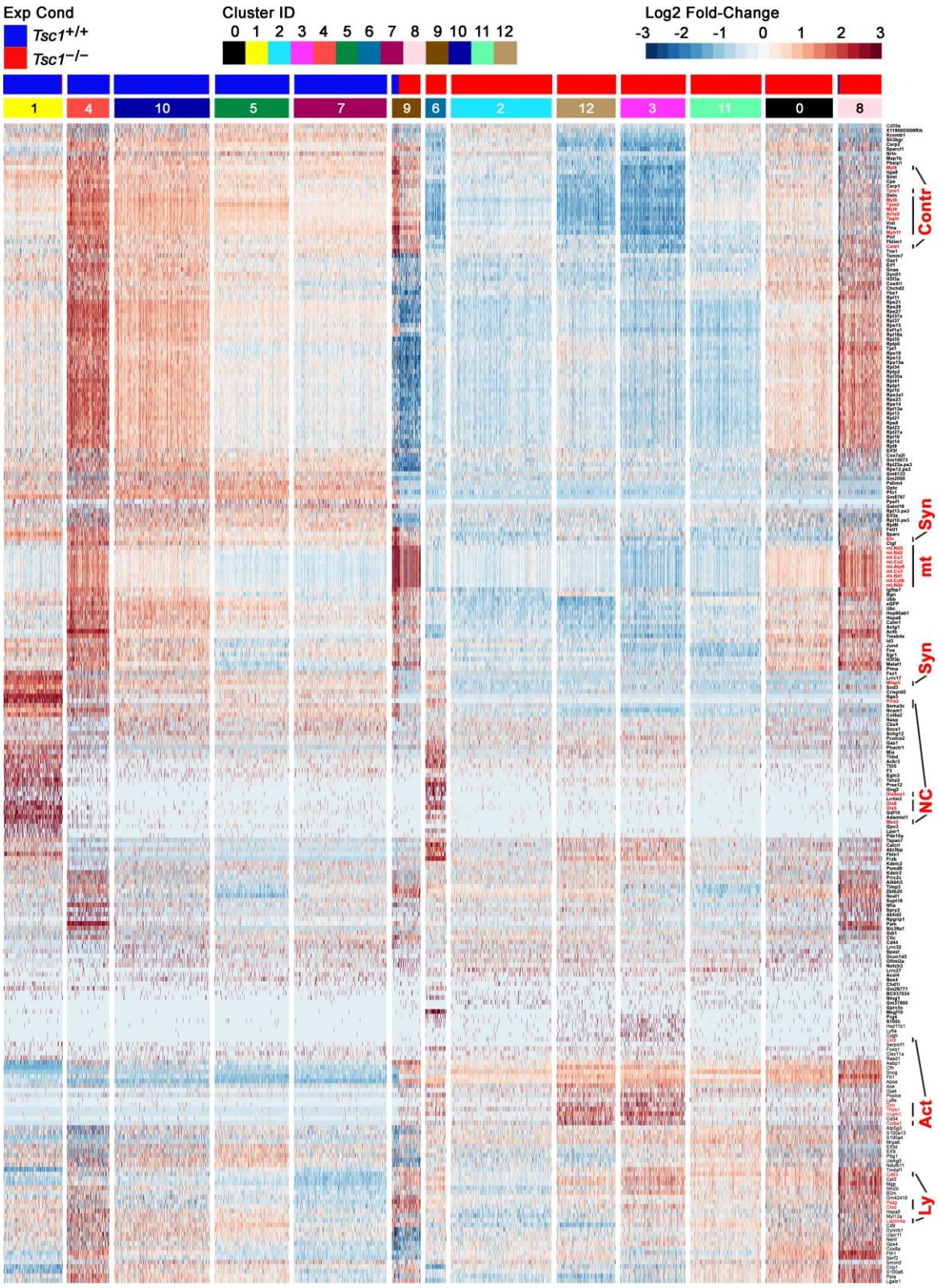

Supplemental Figure 11: Heatmap of the top 250 genes identified by sensitivity mapping from deep learning. *Myh11-CreER^{T2}.mT/mG* (*Tsc1$^{+/+}$*) and *Tsc1$^{fl/fl}$.Myh11-CreER^{T2}.mT/mG* (*Tsc1$^{-/-}$*) mice were treated with tamoxifen at 1.5 wk of age, and single-cell RNA-seq of thoracic aorta GFP^{+} SMCs was performed at 24 wk. Deep learning identified discriminating genes and determined cell clusters. Selected genes (highlighted in red) are annotated as contractile (Contr), synthetic (Syn), mitochondrial (mt), neural crest (NC), SMC activation (Act), and lysosomal (Ly). Marked induction of mitochondrial RNA in Clusters 4, 8, and 9 suggests poor quality or damaged SMCs. High levels of *Prrx2*, *Dlx5*, *Dlx6*, and *Msx2* in Clusters 1 and 6 suggest these SMCs are of neural crest origin.

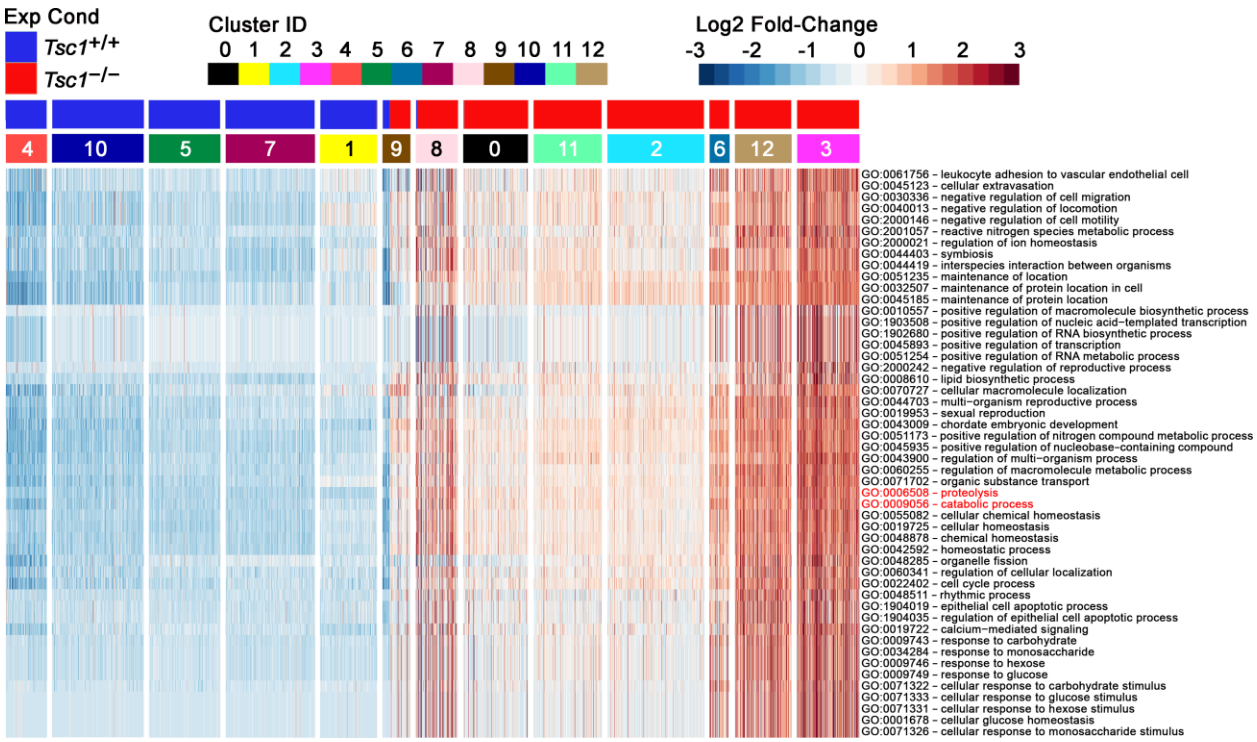

Supplemental Figure 12: Heatmap of the top 50 nGOseq enrichment terms for Cluster 3 by means magnitude of 1st principal component. *Myh11-CreER^{T2}.mT/mG* (*Tsc1$^{+/+}$*) and *Tsc1$^{fl/fl}$.Myh11-CreER^{T2}.mT/mG* (*Tsc1$^{-/-}$*) mice were treated with tamoxifen at 1.5 wk of age, thoracic aortas were procured at 24 wk, GFP^{+} SMCs were isolated by enzymatic digestion and flow cytometry, and single-cell RNA-seq was performed. Deep learning identified discriminating genes and determined cell clusters. Nested GOSeq functional enrichment analysis was performed and the top 50 nGOseq terms are shown with selected processes of interest (proteolysis and catabolic process) are highlighted in red.

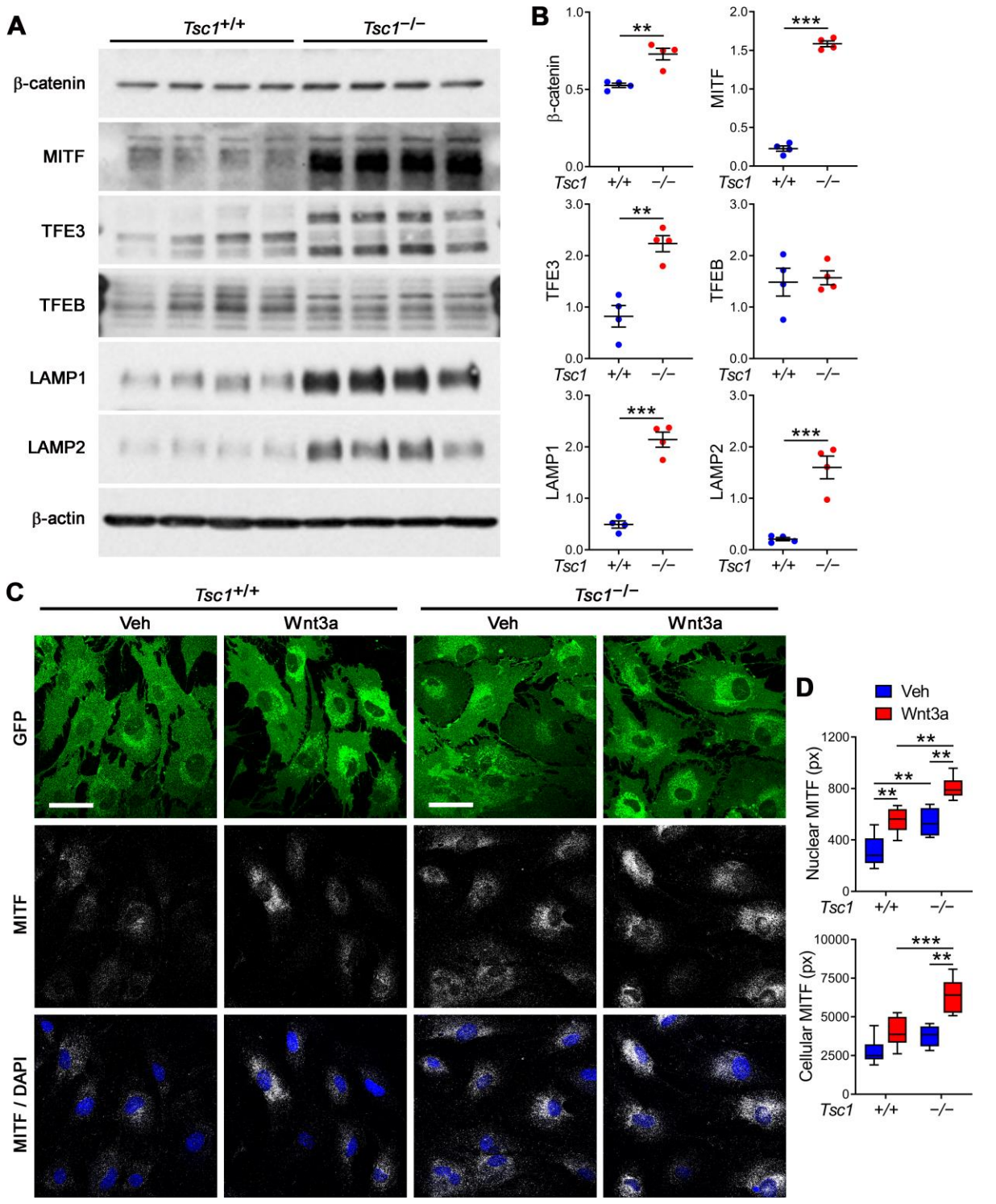

Supplemental Figure 13: Regulation of lysosome biogenesis in SMCs. *Myh11-CreER^{T2}.mT/mG* (*Tsc1$^{+/+}$*) and *Tsc1$^{fl/fl}$.Myh11-CreER^{T2}.mT/mG* (*Tsc1$^{-/-}$*) mice were treated with tamoxifen at 1.5 wk, cells were propagated from enzymatically digested thoracic aortas at 24 wk, and GFP^{+} SMCs were isolated by flow cytometry at P1 and analyzed by P3. (**A**) Expression of selected signaling molecules and lysosome membrane proteins by western blot and (**B**) relative expression to β-actin (n = 4). (**C**) Confocal microscopy for MITF (white) and GFP (green) expression with DAPI-labeled nuclei (blue) of SMCs treated with vehicle (Veh: 0.1% BSA/PBS) or Wnt3a at 100 ng/mL for 2 d (bars = 50 μm) and (**D**) integrated density of nuclear and cellular MITF (n = 6). Data are represented as individual values with mean ± SEM bars or as box-and-whisker plots with interquartile range, median, minimum, and maximum; **P < 0.01, ***P < 0.001, t-test (panel B) or 2-way ANOVA (panel D).

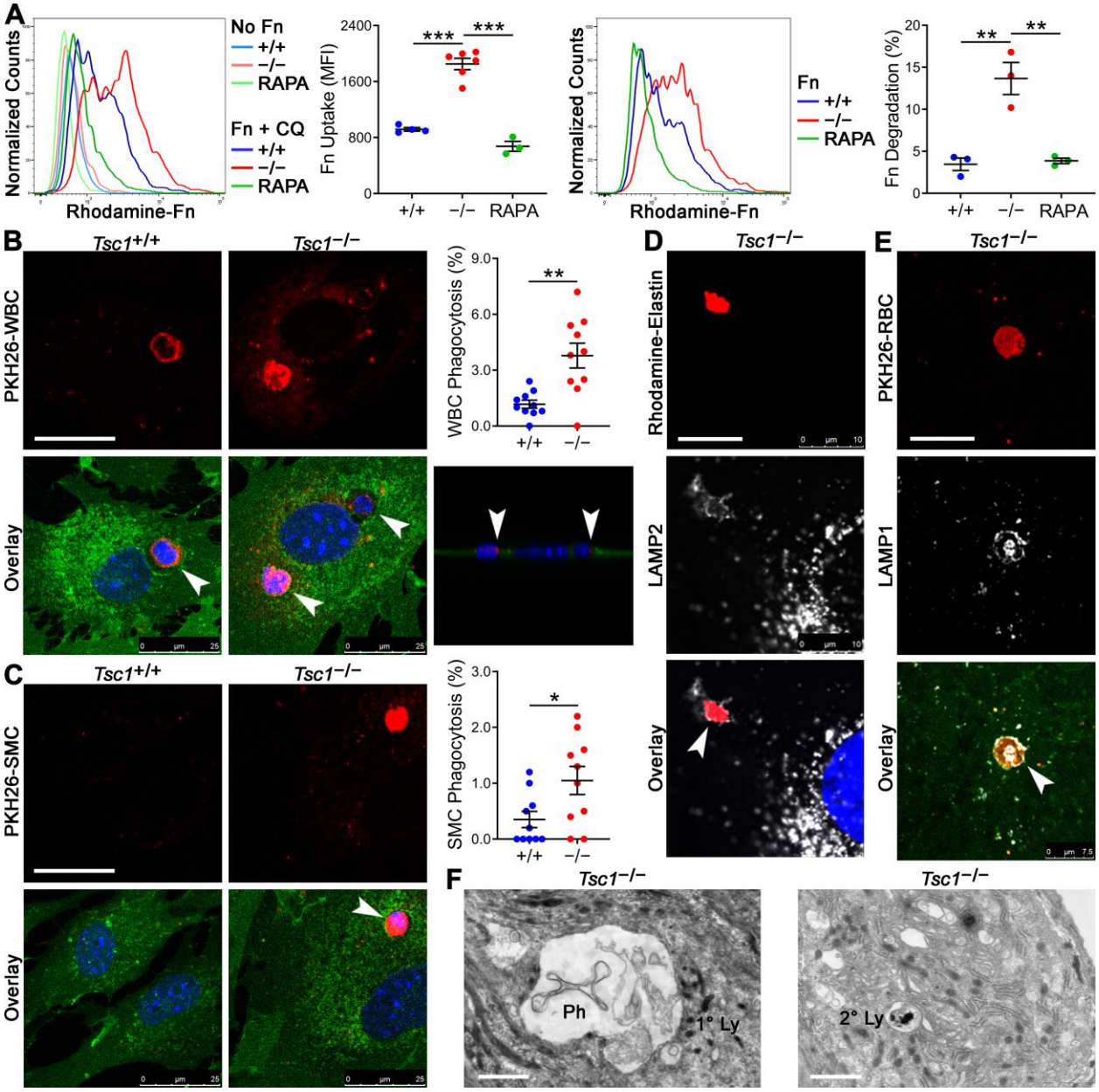

Supplemental Figure 14: SMCs gain degradative functions. SMCs were isolated from thoracic aortas of 24 wk-old, tamoxifen-treated *Myh11-CreER^{T2}.mT/mG* (*Tsc1$^{+/+}$*) and *Tsc1$^{fl/fl}$.Myh11-CreER^{T2}.mT/mG* (*Tsc1$^{-/-}$*) mice, certain of which received rapamycin (RAPA) at 2 mg/kg/d i.p. from 2-24 wk of age. (**A**) Flow cytometry of GFP^{+} SMCs cultured with rhodamine-labeled fibronectin (Fn) with or without chloroquine (CQ) to determine endocytic-dependent accumulation (difference between Fn+CQ vs. No Fn, $n = 3$-6) and concurrent lysosomal degradation (difference between Fn vs. Fn+CQ, $n = 3$). Confocal microscopy of GFP^{+} SMCs (green) cultured with PKH26-labeled, heat-damaged (**B**) leukocytes (WBC) or (**C**) SMCs (red, arrows), (bars = 25 μm); confirmation that leukocytes are intracellular by Z-stack image (arrows); and frequency of GFP^{+} SMCs containing PKH26-labeled leukocytes or SMCs ($n = 10$). Data are represented as individual values with mean ± SEM bars; *$P < 0.05$, **$P < 0.01$, ***$P < 0.001$, 1-way ANOVA (panel A) or t-test (panels B, C)**.** Expression of (**D**) LAMP2 and (**E**) LAMP1 (white) by GFP^{+} SMCs containing rhodamine-elastin or PKH26-erythrocytes (red) within membraned-lined vacuoles (arrows), (bars = 10 μm). (**F**) Transmission electron microscopy of ascending aorta showing infrequent large cytoplasmic vacuole containing debris (left panel) compared to the submicron size of typical organelles (right panel); Ph, phagosome; 1° Ly, primary lysosome; 2° Ly, secondary lysosome (bars = 1 μm).

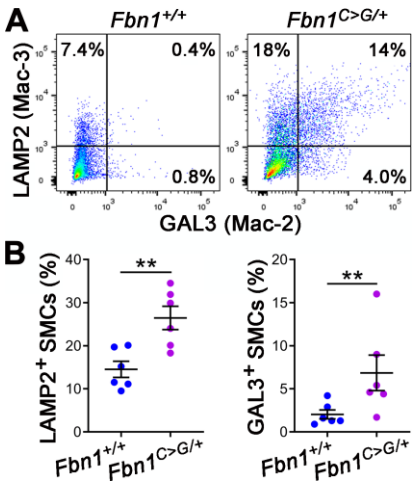

Supplemental Figure 15: Increased degradative SMCs in a murine model of Marfan syndrome. Thoracic aortas were procured from C57BL/6 (*Fbn1*$^{+/+}$) and *Fbn1*$^{C1039G/+}$ (*Fbn1*$^{C>G/+}$) mice at 30 wk of age and cells were isolated by enzymatic digestion. (**A**) Representative flow cytometric analysis of LAMP2 (Mac-3) and GAL3 (Mac-2) expression by SMA^{+} SMCs and (**B**) pooled results from replicates (n = 6). Data are represented as individual values with mean ± SEM bars; **P < 0.01, t-test.

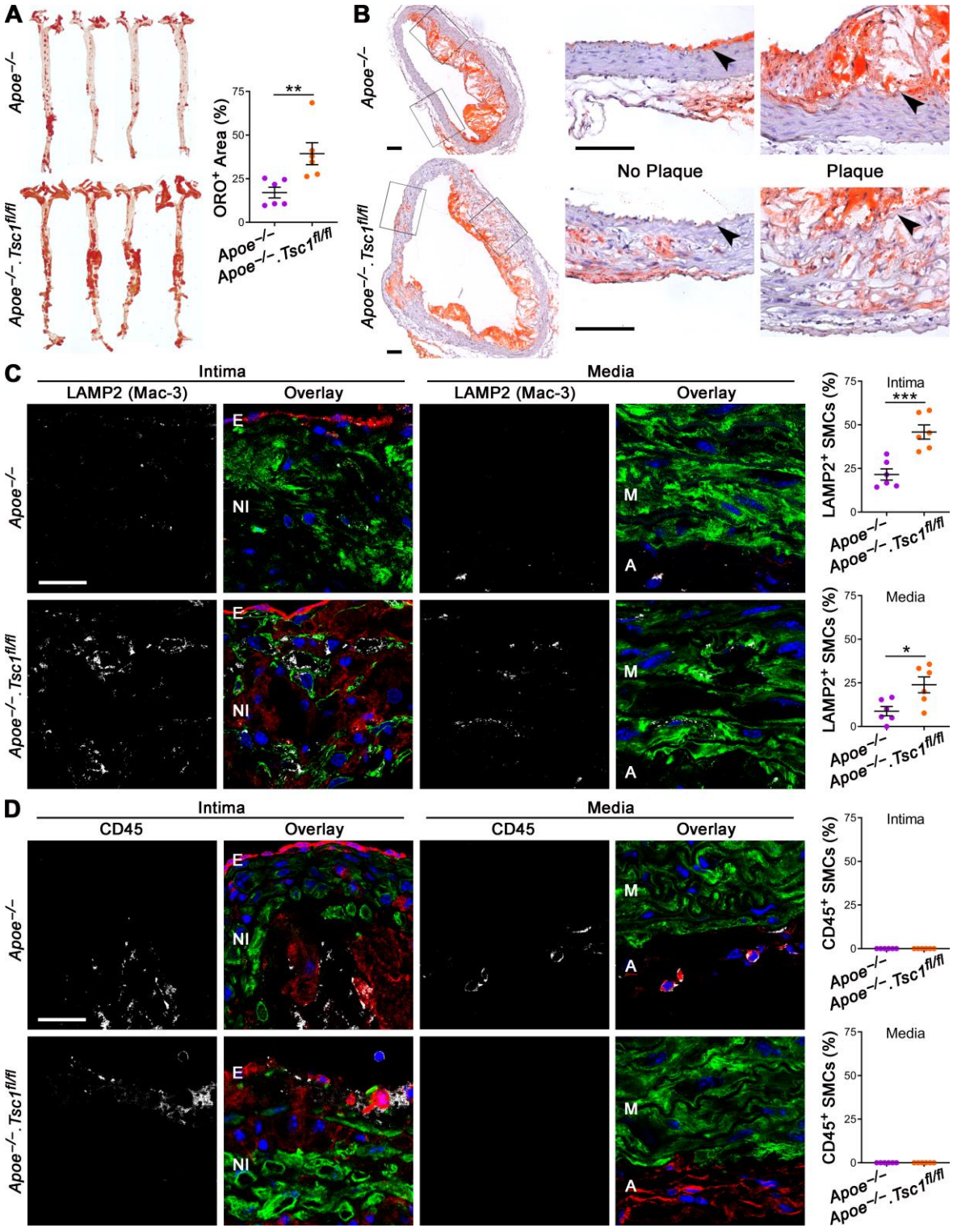

Supplemental Figure 16: SMCs accumulate lipid and express lysosomal but not pan-leukocyte markers in hyperlipidemic mice. *Apoe*$^{-/-}$*.Myh11-CreER*^{T2}*.mT/mG* (*Apoe*$^{-/-}$) and *Apoe*$^{-/-}$*.Tsc1*$^{fl/fl}$*.Myh11-CreER*^{T2}*.mT/mG* (*Apoe*$^{-/-}$*.Tsc1*$^{fl/fl}$) mice were treated with tamoxifen at 7 wk of age, fed a high-fat, high-cholesterol diet from 8 wk, and their aortas were analyzed at 24 wk. (**A**) Oil Red O (ORO) stain of whole aortas and lipid accumulation quantified as % positive area (n = 6). (**B**) Oil Red O stain of ascending aorta sections (bars = 100 μm) with higher magnification of boxed areas showing medial SMCs containing lipid (red) remote or adjacent to intimal atherosclerotic plaques (arrows mark internal elastic lamina). (**C**) Immunostains for LAMP2/Mac-3 (white) and (**D**) CD45 (white) with GFP (green), RFP (red), and DAPI (blue) overlay in ascending aorta intima or media (bars = 25 μm). The endothelium (E), neointima (NI), media (M), and adventitia (A) is labeled and LAMP2 and CD45 expression is quantified as % GFP-mapped SMCs (n = 6). Data are represented as individual values with mean ± SEM bars; *P < 0.05, **P < 0.01, ***P < 0.001, t-test.

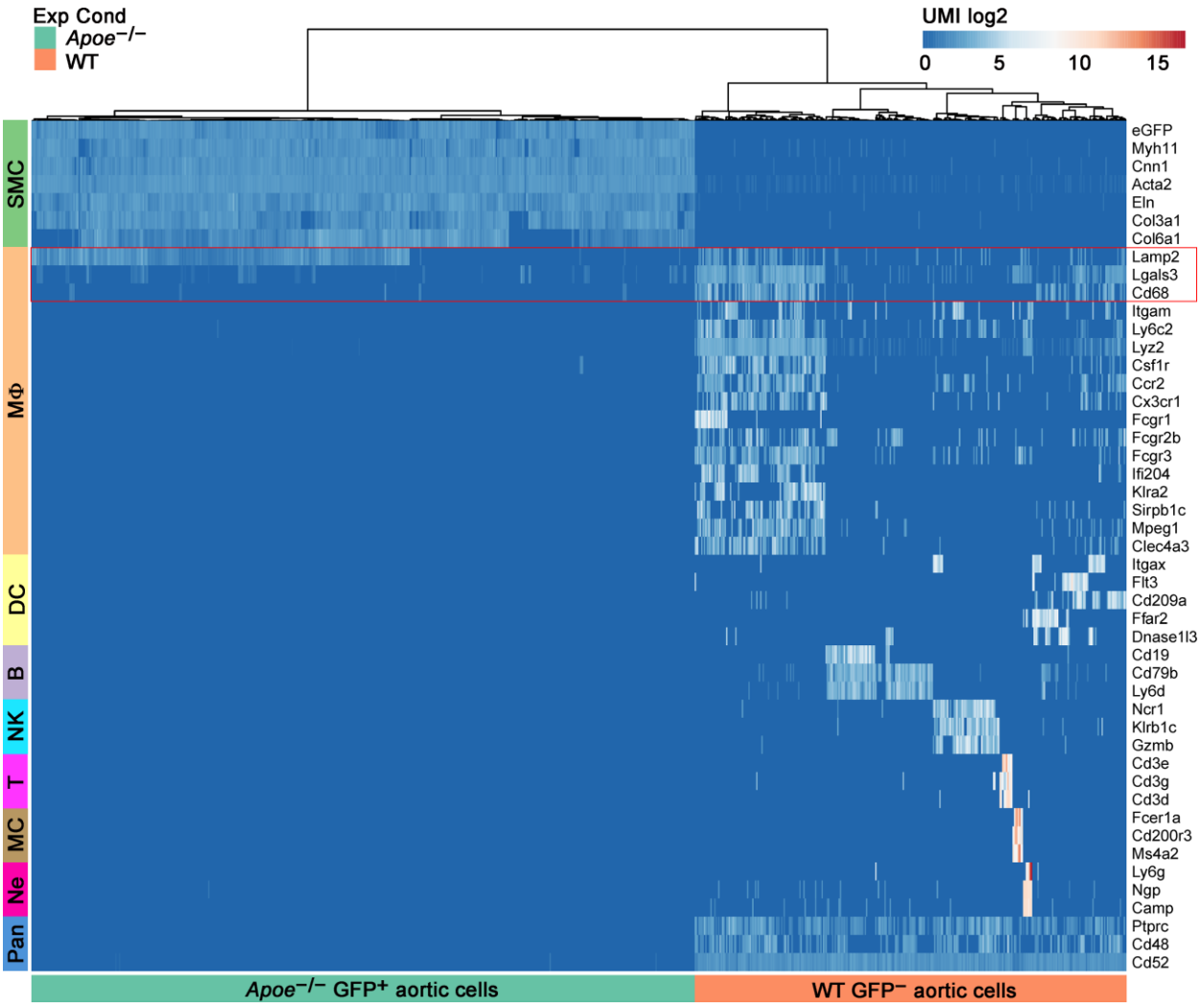

Supplemental Figure 17: Aortic SMCs of hyperlipidemic mice do not express leukocyte transcript markers besides lysosome-related molecules. Cells were enzymatically isolated from thoracic aortas of *Myh11-CreER^{T2}.mT/mG* (WT) and *Apoe$^{-/-}$.Myh11-CreER^{T2}.mT/mG* (*Apoe$^{-/-}$*) mice in which SMCs are fate-mapped by GFP expression. The animals were induced with tamoxifen at 7 wk of age and received a high-fat, high-cholesterol diet from 8 to 24 wk prior to analysis. Single-cell RNA-seq analysis was performed after sorting for GFP expression by flow cytometry. *Apoe$^{-/-}$* GFP^{+} aortic cells (n = 507) clustered entirely separately from WT GFP^{-} aortic cells (n = 330) based on the expression of several SMC, macrophage (MΦ), dendritic cell (DC), B cell, natural killer (NK) cell, T cell, mast cell (MC), neutrophil (Ne), and pan-leukocyte markers. The *Apoe$^{-/-}$* GFP^{+} aortic cells expressed SMC but not leukocyte markers, except for a subset of macrophage markers associated with lysosomes, i.e., *Lamp2, Lgals3*, and *Cd68* that are outlined in red. GFP^{+} cells are identified as SMCs by fate mapping since leaky expression outside of the aortic media or in circulating cells is not detected in our system, whereas a small number of GFP^{-} cells may represent SMCs with incomplete Cre recombination (refer to Supplemental Figure 7C for an example of a rare RFP^{+} medial cell that is CD45^{-} and thus not an infiltrating leukocyte).

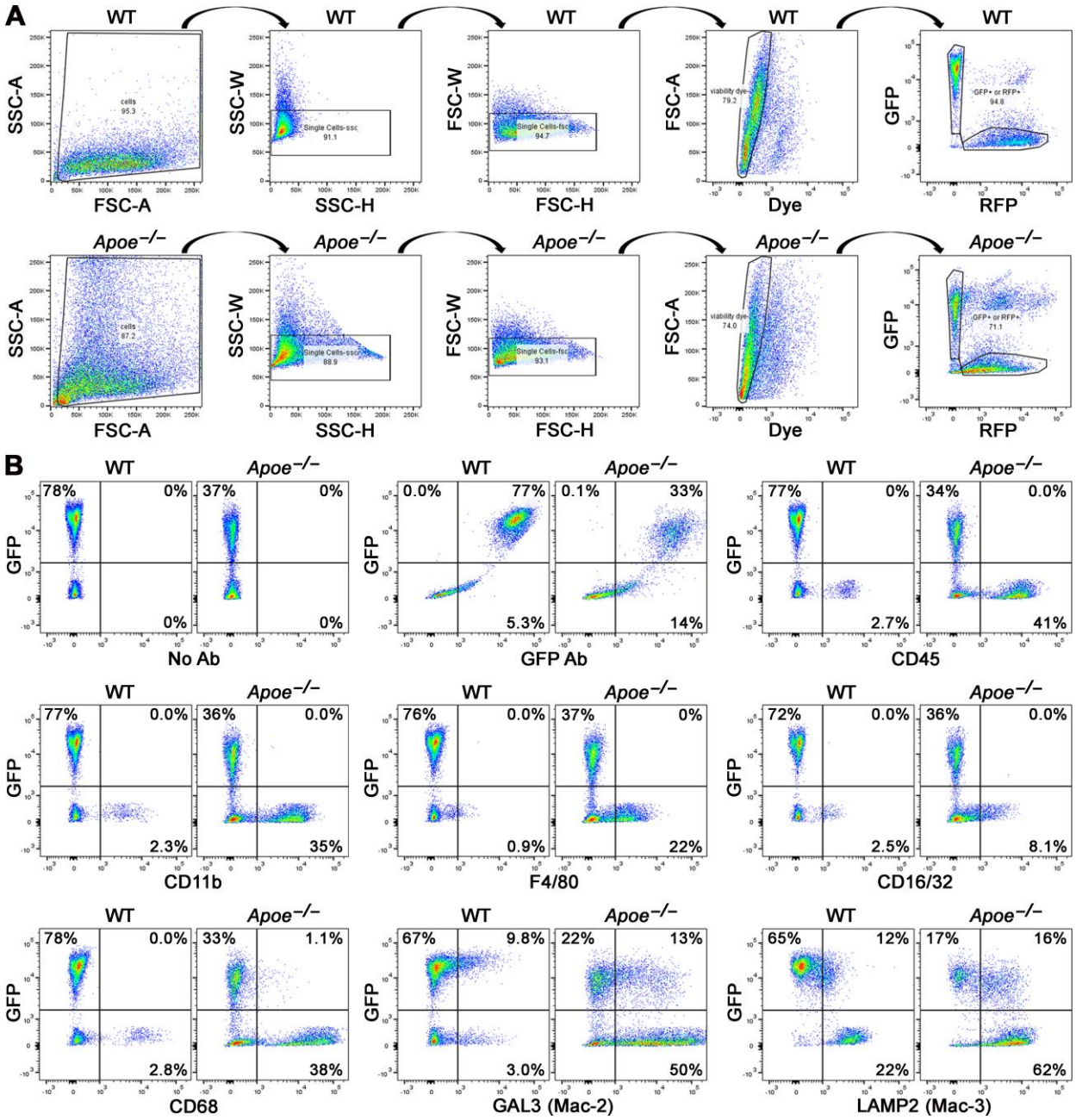

Supplemental Figure 18: Aortic SMCs of hyperlipidemic mice do not express leukocyte protein markers besides lysosome-related molecules. Cells were enzymatically isolated from thoracic aortas of *Myh11-CreER^{T2}.mT/mG* (WT) and *Apoe$^{-/-}$.Myh11-CreER^{T2}.mT/mG* (*Apoe$^{-/-}$*) mice in which SMCs are fate-mapped by GFP expression. The animals were induced with tamoxifen at 7 wk of age and received a high-fat, high-cholesterol diet from 8 to 24 wk prior to analysis. (**A**) Cells were selected by sequential gating of (i) side and forward scatter area (SSC-A and FSC-A) to exclude small debris and dead cells, (ii) SSC and FSC width (W) and height (H) to exclude cell doublets, (iii) uptake of cell impermeant dye to exclude dead and dying cells, and (iv) GFP or RFP single expressors to exclude double negative and double positive cells and particles. (**B**) Controls included no antibody (Ab) and GFP antibody. CD45, CD11b (aka Mac-1a), F4/80, and CD16/CD32 (FcγRIII/FcγRIIB) were not detected in GFP$^+$ SMCs but were expressed by GFP$^-$ cells. In contrast, both GFP$^+$ and GFP$^-$ cells expressed varying levels of LAMP2 (Mac-3), GAL3 (Mac-2), and CD68 (aka LAMP4). The results are representative of 3 independent experiments.

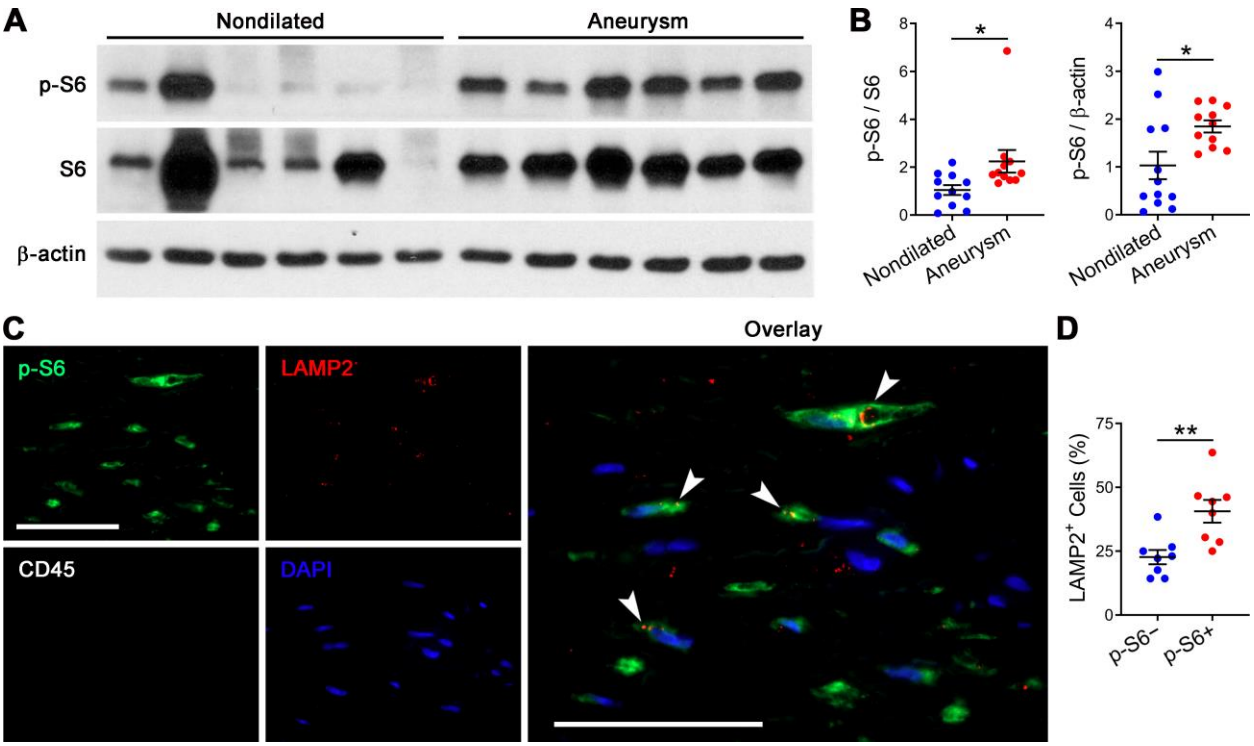

Supplemental Figure 19: mTOR-activated SMCs with degradative phenotype in human TAAD. Ascending aortas were procured from subjects undergoing aortic surgery (Aneurysm) or from organ donors (Nondilated). (**A**) Western blot for mTOR signaling effector in the media from mid-ascending aortas and (**B**) relative expression of phospho-S6 to S6 or β-actin (n = 11-12). (**C**) Immunofluorescence analysis for p-S6 (green), LAMP2 (red), CD45 (white), DAPI-labeled nuclei (blue), and overlay showing p-S6/LAMP2$^+$ medial cells (arrows) that are not CD45$^+$ leukocytes, (bars = 100 μm). (**D**) Frequency of LAMP2 expression by medial cells without or with detectable p-S6 expression (n = 8). Data are represented as individual values with mean ± SEM bars; *P < 0.05, **P < 0.01, t-test.

Supplemental Tables

Supplemental Table 1: Summary of metrics calculated from active biomechanical testing at a common fixed pressure of 90 mmHg and group-specific axial stretch values[A]

	Tsc1$^{fl/fl}$ Veh 12 wk *n* = 6	*Tsc1*$^{fl/fl}$ Tmx 12 wk *n* = 5	*Tsc1*$^{+/+}$ Tmx 36 wk *n* = 3	*Tsc1*$^{fl/fl}$ Tmx 36 wk *n* = 3
100 mM KCl				
Loaded configuration				
Relaxed Outer Diameter (μm)	1731 ± 27	1960 ± 56**	1958 ± 141	3109 ± 240*
Contracted Outer Diameter (μm)	1439 ± 30	1850 ± 47***	1738 ± 140	3132 ± 238**
Change in Outer Diameter (%)	-16.8 ± 1.4	-5.5 ± 1.3***	-11.3 ± 0.8	0.8 ± 0.4***
Stress calculations				
Relaxed Circumferential Stretch	1.60 ± 0.03	1.80 ± 0.03**	1.50 ± 0.03	1.32 ± 0.04*
Contracted Circumferential Stretch	1.31 ± 0.01	1.69 ± 0.02***	1.32 ± 0.04	1.33 ± 0.04
Relaxed Circumferential Stress (kPa)	205 ± 11.5	294 ± 10.5***	220 ± 5.2	199 ± 19.3
Contracted Circumferential Stress (kPa)	136 ± 9.2	260 ± 9.3***	169 ± 7.1	199 ± 19.5
Change in Circumferential Stress (%)	-33.5 ± 2.6	-11.3 ± 2.5***	-23.1 ± 1.5	-0.1 ± 0.2***
Active Circumferential Force (mN)	16.7 ± 2.3	6.4 ± 1.3**	16.2 ± 0.8	0.0 ± 0.2***
1 μM PE				
Loaded configuration				
Relaxed Outer Diameter (μm)	1748 ± 32	1963 ± 50**	2011 ± 132	3124 ± 244*
Contracted Outer Diameter (μm)	1309 ± 42	1763 ± 41***	1436 ± 140	3112 ± 242**
Change in Outer Diameter (%)	-25.2 ± 1.5	-10.1 ± 1.2***	-28.9 ± 2.8	-0.4 ± 0.1***
Stress calculations				
Relaxed Circumferential Stretch	1.61 ± 0.03	1.80 ± 0.03**	1.55 ± 0.03	1.33 ± 0.04*
Contracted Circumferential Stretch	1.18 ± 0.03	1.61 ± 0.03***	1.08 ± 0.07	1.32 ± 0.04*
Relaxed Circumferential Stress (kPa)	209 ± 13.5	296 ± 12.9**	233 ± 3.2	202 ± 20.4
Contracted Circumferential Stress (kPa)	110 ± 9.8	235 ± 12.1***	109 ± 11.7	199 ± 20.3*
Change in Circumferential Stress (%)	-47.8 ± 2.6	-20.4 ± 2.4***	-53.2 ± 4.4	-1.1 ± 0.2***
Active Circumferential Force (mN)	26.8 ± 2.9	12.4 ± 1.6**	49.3 ± 4.9	1.4 ± 0.2***

[A] *Tsc1*$^{fl/fl}$*.Myh11-CreER*^{T2}*.mT/mG* mice were treated with tamoxifen (Tmx) or vehicle (Veh) at 1.5 wk of age and their aortas were analyzed at 12 wk. Additionally, *Tsc1*$^{fl/fl}$*.Myh11-CreER*^{T2}*.mT/mG* (*Tsc1*$^{-/-}$) and *Myh11-CreER*^{T2}*.mT/mG* (*Tsc1*$^{+/+}$) mice were treated with tamoxifen at 1.5 wk of age and their aortas were analyzed at 36 wk. Ascending segments were stimulated *ex vivo* with 100 mM KCl or 1 μM phenylephrine (PE) and allowed to contract under a constant load to evaluate effects of SMC-specific disruption of *Tsc1* on tissue-level contractility. Metrics were calculated at "relaxed" (i.e. prior to agonist addition) and "contracted" (i.e. 15 min following stimulation) states as well as the maximum percentage change from relaxed state. Impaired contractile response to KCl and PE may be interpreted as a loss in contractile strength, whereas a loss of contractile capability to one agonist alone may be interpreted as a signaling impairment without loss of contractile strength. By this interpretation, ascending aortas from Tmx and *Tsc1*$^{-/-}$ mice showed marked loss of contractile strength compared to controls as evaluated by percentage change in outer diameter and circumferential stress. This observation was independent of age, though observations were more severe in the 36 wk group as contractile response was nearly completely ablated. Data represent mean ± SEM; **P* < 0.05, ***P* < 0.01, ****P* < 0.001, t-test.

Supplemental Table 2: Summary of metrics calculated from passive biomechanical testing at a common fixed pressure of 100 mmHg and group-specific axial stretch values[A]

	Ascending				Descending			
	Tsc1$^{fl/fl}$	*Tsc1*$^{fl/fl}$	*Tsc1*$^{+/+}$	*Tsc1*$^{fl/fl}$	*Tsc1*$^{fl/fl}$	*Tsc1*$^{fl/fl}$	*Tsc1*$^{+/+}$	*Tsc1*$^{fl/fl}$
	Veh	Tmx	Tmx	Tmx	Veh	Tmx	Tmx	Tmx
	12 wk	12 wk	36 wk	36 wk	12 wk	12 wk	36 wk	36 wk
	n = 5	*n* = 7	*n* = 3	*n* = 3	*n* = 5	*n* = 7	*n* = 3	*n* = 3
Unloaded dimensions								
Wall Thickness (μm)	119 ± 3.1	127 ± 6.0	124 ± 6.6	179 ± 10.3*	115 ± 4.3	118 ± 3.0	116 ± 2.5	191 ± 48.5
Outer Diameter (μm)	1226 ± 28	1128 ± 29*	1392 ± 69	2481 ± 237*	961 ± 13	810 ± 17***	1056 ± 33	1355 ± 243
Axial Length (mm)	2.88 ± 0.10	2.68 ± 0.06	3.41 ± 0.09	4.74 ± 0.38*	6.51 ± 0.50	5.30 ± 0.21*	5.41 ± 0.30	7.25 ± 0.71
Loaded dimensions (at P = 100 mmHg)								
Outer Diameter (μm)	1963 ± 60.3	1830 ± 45.0	2181 ± 103.2	3234 ± 195.1**	1559 ± 27.7	1385 ± 22.0***	1672 ± 51.0	2035 ± 194.6
Wall Thickness (μm)	39 ± 1.3	41 ± 2.4	41 ± 3.4	78 ± 1.5***	43 ± 1.0	42 ± 1.7	45 ± 2.1	83 ± 18.2
Inner Radius (μm)	943 ± 31.3	875 ± 20.4	1049 ± 48.3	1539 ± 97.4*	736 ± 13.1	651 ± 11.0***	790 ± 26.3	935 ± 96.5
In Vivo Axial Stretch (λ_z^{iv})	1.77 ± 0.06	1.77 ± 0.06	1.80 ± 0.05	1.67 ± 0.00	1.48 ± 0.03	1.47 ± 0.02	1.47 ± 0.05	1.32 ± 0.05
In Vivo Circumferential Stretch (λ_ϑ)	1.74 ± 0.04	1.79 ± 0.03	1.69 ± 0.03	1.39 ± 0.07*	1.79 ± 0.03	1.95 ± 0.04*	1.73 ± 0.09	1.77 ± 0.21
Systolic Cauchy Stresses (kPa)								
Circumferential, σ_ϑ	327 ± 20.2	292 ± 12.4	343 ± 14.2	265 ± 17.3*	226 ± 3.9	211 ± 10.2	233 ± 15.2	171 ± 47.4
Axial, σ_z	302 ± 13.7	215 ± 10.2***	282 ± 15.4	186 ± 8.2**	175 ± 5.1	153 ± 8.7	167 ± 10.5	118 ± 37.2
Systolic Linearized Stiffness (MPa)								
Circumferential, $C_{\vartheta\vartheta\vartheta\vartheta}$	2.01 ± 0.08	2.10 ± 0.10	2.78 ± 0.13	4.58 ± 0.24**	1.81 ± 0.15	1.96 ± 0.45	1.66 ± 0.24	3.67 ± 0.33**
Axial, C_{zzzz}	1.59 ± 0.13	1.08 ± 0.05**	1.44 ± 0.05	1.39 ± 0.19	2.27 ± 0.12	1.79 ± 0.10*	1.58 ± 0.33	1.44 ± 0.52
Distensibility (1/MPa)	24.66 ± 1.75	33.22 ± 2.07*	16.81 ± 0.14	11.43 ± 1.89*	18.12 ± 1.66	29.59 ± 3.54*	20.15 ± 1.66	9.99 ± 3.67
Systolic Stored Energy (kPa)	98 ± 6.1	72 ± 4.8**	83 ± 3.6	37 ± 1.2***	56 ± 1.4	47 ± 3.2*	52 ± 5.8	25 ± 11.8

[A] *Tsc1*$^{fl/fl}$*.Myh11-CreER*^{T2}*.mT/mG* mice were treated with tamoxifen (Tmx) or vehicle (Veh) at 1.5 wk of age and their aortas were analyzed at 12 wk. Additionally, *Tsc1*$^{fl/fl}$*.Myh11-CreER*^{T2}*.mT/mG* (*Tsc1*$^{-/-}$) and *Myh11-CreER*^{T2}*.mT/mG* (*Tsc1*$^{+/+}$) mice were treated with tamoxifen at 1.5 wk of age and their aortas were analyzed at 36 wk. Biomechanical testing was performed on ascending and descending thoracic segments under passive (i.e. no contribution from smooth muscle) conditions to evaluate material and structural changes in thoracic aortic segments following SMC-specific disruption of *Tsc1*. Unloaded conditions were determined under no axial load and atmospheric pressure. Loaded geometry, stress, stiffness, and stored energy were evaluated at a common pressure of 100 mmHg and group-specific axial stretches. *Tsc1* disruption induced few changes in the ascending aorta at 12 wk whereas many changes were observed at 36 wk including growth (increased unloaded diameter and thickness), material stiffening (increased linearized stiffness), structural stiffening (decreased distensibility), and loss of energy storage capacity. Similar observations were observed in the 36 wk descending thoracic aorta segments, though not as severe, and results were not statistically significant excepting an increase in circumferential stiffness. Increased linearized circumferential stiffness has been shown to correlate with aneurysm development in the ascending aorta. Decreased energy storage capacity is particularly significant in the ascending aorta where energy is stored during systole and released during diastole to augment blood flow. Data represent mean ± SEM; *P < 0.05, **P < 0.01, ***P < 0.001, t-test.

Supplemental Table 3: Gene expression by bulk RNA-seq[A]

Symbol	logFC	logCPM	pvals	padj	*Tsc1* $^{+/+}$	*Tsc1* $^{+/+}$	*Tsc1* $^{+/+}$	*Tsc1* $^{+/+}$	*Tsc1* $^{-/-}$	*Tsc1* $^{-/-}$	*Tsc1* $^{-/-}$	*Tsc1* $^{-/-}$
Kcnt1	5.5	4.5	1.1E-98	1.7E-94	0.6	1.6	0.7	1.1	58.1	31.9	44.3	41.3
Slc6a17	3.0	6.5	3.6E-98	2.7E-94	16.0	23.7	16.8	22.0	154.4	163.7	168.5	148.5
Kcnk3	3.8	6.9	1.6E-90	7.8E-87	17.7	14.8	12.1	18.8	254.5	173.9	254.6	180.7
Gm6969	-6.0	3.1	4.6E-85	1.7E-81	17.4	18.1	15.3	14.9	0.1	0.4	0.1	0.4
Gpnmb	3.3	6.5	9.6E-77	2.9E-73	15.1	16.8	18.6	17.0	206.8	142.7	183.2	114.1
Pcna-ps2	-5.7	2.5	1.4E-71	3.5E-68	10.5	10.7	12.3	10.9	0.2	0.2	0.1	0.3
Ptgds	6.4	3.9	2.7E-67	5.8E-64	0.3	0.7	0.2	0.3	39.6	20.3	39.2	18.7
Gm45847	7.1	3.3	9.3E-67	1.7E-63	0.1	0.2	0.1	0.2	27.7	15.1	25.2	11.7
Eno1b	-4.9	4.6	4.9E-64	8.1E-61	63.9	29.6	31.6	61.6	1.2	1.6	1.9	1.2
Gm14305	6.6	2.7	2.1E-62	3.1E-59	0.0	0.0	0.3	0.0	10.9	16.3	11.0	13.3
Rragd	3.8	4.4	3.6E-62	5.0E-59	2.1	3.5	2.5	3.3	47.8	30.0	47.3	29.5
Npy4r	3.0	4.3	1.0E-59	1.3E-56	3.8	5.6	3.2	5.0	31.6	34.5	35.3	35.6
Nkd2	2.9	4.8	3.2E-57	3.7E-54	6.2	7.4	6.8	6.2	59.8	43.1	56.7	36.1
Uap1l1	2.1	5.4	2.7E-53	2.8E-50	13.8	19.8	16.9	16.8	70.6	69.0	78.0	63.3
Dpp7	1.9	5.4	9.6E-53	9.5E-50	20.0	17.1	20.0	17.5	72.7	67.7	66.9	62.2
Vstm2b	-3.8	3.3	1.6E-51	1.5E-48	14.5	14.3	22.3	20.6	1.4	1.3	1.2	1.3
Sox4	3.3	7.3	2.1E-49	1.8E-46	22.7	32.2	23.0	38.9	363.3	223.6	347.9	218.6
Kif1a	1.9	7.4	3.0E-48	2.5E-45	66.4	75.7	68.1	69.3	244.0	292.7	283.0	250.2
Chdh	3.7	4.9	5.3E-47	4.1E-44	6.8	3.2	2.7	4.2	66.2	46.7	62.3	39.1
Sbk1	2.1	5.0	1.4E-46	1.0E-43	13.4	12.3	10.9	14.2	53.9	44.4	60.7	51.8
Tpd52l1	2.1	4.4	3.5E-44	2.5E-41	8.8	8.7	7.7	6.9	37.6	32.1	35.2	30.4
Cpm	3.2	3.6	1.3E-43	8.9E-41	2.1	2.6	1.5	2.9	25.3	17.0	24.5	19.5
Vwa1	-2.0	4.8	1.9E-42	1.2E-39	36.8	42.8	46.9	51.5	10.7	10.8	10.5	12.1
Casq1	-3.9	5.8	2.4E-42	1.5E-39	104.6	85.2	122.6	91.9	2.7	9.8	4.7	9.1
Sncg	2.9	7.2	1.0E-38	6.0E-36	41.8	36.3	29.3	35.3	367.7	198.5	320.1	173.7
Ifit2	1.6	5.5	3.9E-38	2.3E-35	22.1	23.6	19.8	19.3	69.6	69.4	56.2	69.5
Pcsk5	-2.2	4.9	6.2E-38	3.4E-35	59.9	40.9	56.2	42.7	9.4	13.7	9.2	11.0
Gm9899	3.9	2.6	1.5E-37	8.1E-35	0.8	0.5	0.9	0.7	13.8	9.4	14.1	7.5
Tnfrsf11b	2.7	5.9	2.2E-37	1.1E-34	15.2	17.4	15.7	14.7	131.1	65.4	144.0	78.6
Zfp973	4.8	1.5	2.7E-37	1.3E-34	0.2	0.4	0.1	0.0	6.3	4.5	5.3	5.2
Tcn2	1.7	6.7	6.5E-37	3.2E-34	50.6	48.9	52.3	45.9	174.8	139.1	177.3	134.7
Atp1b1	3.1	6.9	1.7E-36	8.1E-34	19.2	31.0	22.9	28.4	301.8	151.5	266.3	137.9
Sesn3	1.5	6.9	3.4E-36	1.5E-33	57.7	68.0	56.8	61.0	168.8	165.9	187.8	174.5
Mamdc2	2.8	6.0	5.4E-36	2.4E-33	11.0	23.1	11.9	19.4	129.9	97.7	142.5	88.7
Gm4735	-4.5	3.5	2.5E-35	1.1E-32	30.5	14.1	14.4	29.4	1.5	0.4	1.0	1.2
Nxph3	3.2	3.8	2.7E-34	1.1E-31	1.8	3.3	2.2	3.3	31.1	18.5	31.4	18.0
Asb10	3.6	3.2	5.7E-34	2.3E-31	1.0	2.0	0.7	2.0	15.8	17.1	15.4	17.7
Meg3	-1.6	6.9	8.0E-34	3.1E-31	203.7	182.3	169.5	190.9	70.0	60.8	60.1	48.9
Gpr137b-ps	3.0	3.2	2.6E-33	1.0E-30	1.7	1.4	2.1	2.6	18.0	17.5	11.2	17.2

[A] *Myh11-CreER^{T2}.mT/mG* (*Tsc1$^{+/+}$*) and *Tsc1$^{fl/fl}$.Myh11-CreER^{T2}.mT/mG* (*Tsc1$^{-/-}$*) mice were treated with tamoxifen at 1.5 wk and the thoracic aortas were analyzed by bulk RNA-seq at 24 wk (n = 4 aortas in each group). Gene expression was quantified, read counts were normalized, and differentially expressed genes were identified. The top 40 gene expression changes are shown; the complete table for 14,944 selected genes is appended to GSE135177 deposited in Gene Expression Omnibus.

Supplemental Table 4: Gene expression by single-cell RNA-seq[A]

Symbol	Med_*Tsc1* $^{-/-}$	Med_*Tsc1* $^{+/+}$	Min_*Tsc1* $^{-/-}$	Min_*Tsc1* $^{+/+}$	Max_*Tsc1* $^{-/-}$	Max_*Tsc1* $^{+/+}$
Apoe	4.9451	0.0000	0.0000	0.0000	11.6002	11.2311
Sncg	4.0945	0.0000	0.0000	0.0000	9.7700	6.1059
Gpx3	3.6232	0.0000	0.0000	0.0000	9.6774	4.8585
Rnase4	2.5410	0.0000	0.0000	0.0000	7.5576	4.2403
Cfh	3.2634	1.1665	0.0000	0.0000	9.0665	7.2185
Ank	2.0462	0.0000	0.0000	0.0000	5.4634	5.1583
Mgp	7.9674	5.9572	3.9585	0.0000	16.9349	12.7365
Ftl1	5.8588	3.8556	2.5509	0.0000	13.4777	16.3785
Chchd10	1.9867	0.0000	0.0000	0.0000	5.6940	3.5599
Mgst1	1.8914	0.0000	0.0000	0.0000	5.0186	4.9441
Sox4	1.8808	0.0000	0.0000	0.0000	6.6741	5.5829
Atp1b1	1.8543	0.0000	0.0000	0.0000	5.7512	3.2902
Lgals3	1.7215	0.0000	0.0000	0.0000	7.6021	8.7820
Sepp1	3.6196	2.0573	0.0000	0.0000	8.5522	5.4664
Kcnk3	1.4675	0.0000	0.0000	0.0000	4.9197	4.5188
Gpnmb	1.4616	0.0000	0.0000	0.0000	5.4266	3.2299
Slc6a6	1.4596	0.0000	0.0000	0.0000	8.1805	5.1501
Scn1b	1.3809	0.0000	0.0000	0.0000	5.0919	5.0421
Tulp4	1.3617	0.0000	0.0000	0.0000	5.4071	3.9569
Gns	1.3492	0.0000	0.0000	0.0000	4.7842	4.4330
Mt2	2.7805	1.4393	0.0000	0.0000	8.1156	7.7667
Mt1	4.4382	3.1066	0.0000	0.0000	9.5280	8.7467
Tmsb10	3.7927	2.4617	0.0000	0.0000	8.4839	12.6254
Cdo1	2.5159	1.1894	0.0000	0.0000	5.9513	5.5695
Itgbl1	2.1382	0.8308	0.0000	0.0000	6.2456	5.8200
Tmcc3	1.3067	0.0000	0.0000	0.0000	4.5038	4.2178
Plbd2	1.2955	0.0000	0.0000	0.0000	6.1205	3.6995
Dkk3	3.0428	1.7485	0.0000	0.0000	7.8741	5.6803
Ppp1r14b	1.2913	0.0000	0.0000	0.0000	6.1726	3.2699
Frzb	1.2801	0.0000	0.0000	0.0000	6.6175	6.3089
Glul	1.2408	0.0000	0.0000	0.0000	5.4704	4.2822
Map4k4	1.2358	0.0000	0.0000	0.0000	4.5566	4.1435
Cst3	6.0350	4.8025	2.4470	0.0000	13.5430	10.8299
Nbl1	2.3191	1.0922	0.0000	0.0000	5.4884	5.6860
Slc6a8	1.2220	0.0000	0.0000	0.0000	4.1859	3.5535
Phlda3	1.2092	0.0000	0.0000	0.0000	5.3707	5.2248
Igfbp5	1.2074	0.0000	0.0000	0.0000	8.2875	5.5309
Dnajc1	1.2044	0.0000	0.0000	0.0000	4.7731	4.2345
Myo1d	1.2017	0.0000	0.0000	0.0000	4.7842	4.0327
Slc5a3	1.1890	0.0000	0.0000	0.0000	7.5292	5.9665

[A] *Myh11-CreER^{T2}.mT/mG* (*Tsc1$^{+/+}$*) and *Tsc1$^{fl/fl}$.Myh11-CreER^{T2}.mT/mG* (*Tsc1$^{-/-}$*) mice were treated with tamoxifen at 1.5 wk and isolated GFP^{+} SMCs from thoracic aortas were analyzed by single-cell RNA-seq at 24 wk (*n* = 2,788 cells from 2 aortas). Cell barcodes and UMIs were identified, quantification was performed using UMI-tools count function to find the number of unique UMIs mapping to each gene, raw count data was filtered, and finalized read counts were normalized. The top 40 gene expression changes are shown; the complete table for 10,292 selected genes is appended to GSE135240 deposited in Gene Expression Omnibus.

Supplemental Table 5: Nested GOSeq functional enrichment of bulk RNA-seq data[A]

Class	Accession	Term	k	M	n	N	Pvalue
CC	GO:0044391	ribosomal subunit	77	270	95	1277	4.6E-28
CC	GO:0005840	ribosome	80	270	108	1277	1.4E-25
CC	GO:0015934	large ribosomal subunit	47	270	56	1277	9.1E-19
CC	GO:0030529	intracellular ribonucleoprotein complex	84	270	151	1277	8.2E-17
BP	GO:2000273	positive regulation of receptor activity	2	59	4	175	2.6E-15
CC	GO:0030529	intracellular ribonucleoprotein complex	79	92	104	191	2.1E-11
BP	GO:0006612	protein targeting to membrane	2	59	4	175	2.5E-10
CC	GO:0030529	intracellular ribonucleoprotein complex	39	99	52	348	1.0E-09
CC	GO:0015935	small ribosomal subunit	31	270	41	1277	1.7E-09
CC	GO:0030529	intracellular ribonucleoprotein complex	45	153	72	604	3.3E-09
CC	GO:0043228	non-membrane-bounded organelle	83	92	124	191	1.2E-08
CC	GO:0030529	intracellular ribonucleoprotein complex	49	279	87	1094	1.5E-08
BP	GO:1904181	positive regulation of membrane depolarization	2	59	3	175	2.9E-08
CC	GO:0030529	intracellular ribonucleoprotein complex	51	521	107	2095	1.3E-07
CC	GO:0030529	intracellular ribonucleoprotein complex	52	651	113	2700	1.7E-07
BP	GO:0042254	ribosome biogenesis	35	327	64	1466	3.1E-07
CC	GO:0005730	nucleolus	44	270	101	1277	8.7E-07
CC	GO:0043228	non-membrane-bounded organelle	139	270	471	1277	8.9E-07
CC	GO:0005730	nucleolus	24	97	35	343	1.8E-06
CC	GO:0030529	intracellular ribonucleoprotein complex	53	675	123	2648	3.2E-06
CC	GO:0030529	intracellular ribonucleoprotein complex	110	1060	393	5496	5.0E-06
BP	GO:0006364	rRNA processing	20	327	31	1466	5.5E-06
MF	GO:0003676	nucleic acid binding	69	78	112	169	6.6E-06
CC	GO:0033176	proton-transporting V-type ATPase complex	11	1060	16	5496	1.5E-05
CC	GO:0030529	intracellular ribonucleoprotein complex	72	1252	225	5892	3.9E-05
BP	GO:0042274	ribosomal small subunit biogenesis	15	327	21	1466	4.2E-05
CC	GO:0005730	nucleolus	31	84	47	204	6.2E-05
MF	GO:0003723	RNA binding	73	146	129	411	6.7E-05
MF	GO:1901363	heterocyclic compound binding	82	146	157	411	6.9E-05
CC	GO:0005730	nucleolus	28	154	55	613	1.3E-04

[A]Functional enrichment analysis was performed on the differentially expressed genes with false discovery rate corrected *P* values ≤ 0.01 of the bulk RNA-seq dataset. The analysis used all possible annotated genes as the background distributions. Briefly, GOseq analysis was performed to identify enriched gene ontology (GO) terms. Nested GOseq (nGOseq), a modified version of the nested Expression Analysis Systematic Explorer (nEASE) algorithm, was then used to identify enriched nested GO (nGO) terms driving the statistical enrichment of upper-level GOseq terms. The top 30 nGOseq accessions and terms are shown; the complete table is appended to GSE135177 deposited in Gene Expression Omnibus.

Supplemental Table 6: Nested GOSeq functional enrichment of single-cell RNA-seq data[A]

Class	Accession	Term	k	M	n	N	Pvalue
CC	GO:0005634	nucleus	156	500	1734	9023	1.3E-11
CC	GO:0016020	membrane	379	723	5502	13465	1.8E-11
CC	GO:0009986	cell surface	58	723	465	13465	6.7E-10
BP	GO:0003008	system process	95	393	803	5926	8.7E-10
BP	GO:0003008	system process	81	442	798	8342	9.1E-10
CC	GO:0009986	cell surface	57	713	460	13358	9.4E-10
CC	GO:0043231	intracellular membrane-bounded organelle	291	500	4118	9023	1.8E-09
CC	GO:0044425	membrane part	202	517	2818	10054	5.6E-09
CC	GO:0043227	membrane-bounded organelle	315	500	4600	9023	6.3E-09
CC	GO:0044425	membrane part	222	555	3193	10759	1.9E-08
CC	GO:0044425	membrane part	262	723	3710	13465	2.5E-08
CC	GO:0044425	membrane part	259	713	3687	13358	2.7E-08
BP	GO:0003008	system process	90	569	976	10362	1.0E-07
BP	GO:0003008	system process	80	482	856	8902	1.2E-07
BP	GO:0010761	fibroblast migration	12	528	36	9862	1.7E-07
BP	GO:0003008	system process	48	155	384	2479	1.8E-07
BP	GO:0003008	system process	85	528	947	9862	2.1E-07
BP	GO:0003008	system process	54	175	443	2791	2.1E-07
BP	GO:0003008	system process	69	397	712	7258	2.9E-07
BP	GO:0003008	system process	86	274	830	4299	2.9E-07
CC	GO:0098552	side of membrane	42	723	341	13465	3.0E-07
BP	GO:0003008	system process	53	195	419	2891	3.4E-07
CC	GO:0044425	membrane part	230	627	3289	11665	3.5E-07
CC	GO:0005913	cell-cell adherens junction	15	241	56	3975	3.5E-07
BP	GO:0003008	system process	66	318	653	5584	4.2E-07
CC	GO:0005634	nucleus	113	347	1097	5039	4.2E-07
CC	GO:0044446	intracellular organelle part	137	347	1410	5039	4.7E-07
BP	GO:0003008	system process	82	519	904	9498	5.1E-07
CC	GO:0098552	side of membrane	41	713	340	13358	6.4E-07
BP	GO:0003008	system process	44	200	382	3545	9.5E-07

[A]Functional enrichment analysis was performed on the top 10% most informative genes from sensitivity mapping of single-cell RNA-seq datasets. The analysis used all possible annotated genes as the background distributions. Briefly, GOseq analysis was performed to identify enriched gene ontology (GO) terms. Nested GOseq (nGOseq), a modified version of the nested Expression Analysis Systematic Explorer (nEASE) algorithm, was then used to identify enriched nested GO (nGO) terms driving the statistical enrichment of upper-level GOseq terms. The top 30 nGOseq accessions and terms are shown; the complete table is appended to GSE135240 deposited in Gene Expression Omnibus.

Supplemental Table 7: Gene co-expression in single-cell RNAseq dataset[A]

Gene	*r*	Gene	*r*	Gene	*r*	Gene	*r*	Gene	*r*	Gene	*r*	Gene	*r*
Lamp2	**1.00**	**Ctnnb1**	**1.00**	**Mitf**	**1.00**	**Tfe3**	**1.00**	**Tfeb**	**1.00**	**Myh11**	**1.00**	**Myocd**	**1.00**
Timp2	0.68	Dkk3	0.72	Aebp1	0.22	Ctnnb1	0.29	Myl6	0.20	Flna	0.83	Mylk	0.34
Ctnnb1	0.64	Timp2	0.70	Ctnnb1	0.22	Pmepa1	0.28	Tagln	0.20	Cnn1	0.77	Lpp	0.33
Ftl1	0.62	Aebp1	0.70	Fth1	0.21	Sptbn1	0.27	Dstn	0.20	Tpm1	0.77	Enah	0.31
Psap	0.62	Ank	0.69	Ahnak2	0.21	Lamp2	0.27	eGFP	0.19	Synpo2	0.76	Myh11	0.30
Dkk3	0.62	Itgb5	0.69	Selk	0.20	Tpt1	0.26	Pkm	0.19	Tagln	0.74	Tns1	0.29
Aebp1	0.62	Serf2	0.69	Map1lc3b	0.20	Timp2	0.26	Myl9	0.19	Itga8	0.72	Actn1	0.29
Hexa	0.62	Gabarap	0.67	Nenf	0.20	Ppp1r14b	0.26	Tpm2	0.18	Ppp1r14a	0.72	Tpm1	0.29
Gabarap	0.61	Fth1	0.65	Gabarap	0.20	Serinc3	0.26	Ubc	0.18	Actn1	0.72	Flna	0.29
Lamp1	0.61	Pmepa1	0.65	Timp2	0.20	Zbtb20	0.25	Cpe	0.18	Pbxip1	0.71	Rock1	0.28
Ank	0.59	Bgn	0.65	Serf2	0.20	Ftl1	0.25	Acta2	0.18	Mylk	0.71	Klf6	0.28
Serf2	0.59	Lamp2	0.64	Npdc1	0.20	Gabarap	0.25	Msrb1	0.17	Myl9	0.71	Cald1	0.28
Itm2b	0.58	Ftl1	0.64	Bgn	0.20	Fth1	0.25	Cbr2	0.17	Smtn	0.70	Ttc28	0.28
Cd63	0.58	Atp1b3	0.63	Gpx4	0.20	Lrp1	0.25	Pdlim7	0.17	Myl6	0.70	Egr1	0.28
Gpnmb	0.58	Serinc3	0.63	Cox8a	0.20	Gnai2	0.25	Slc25a4	0.17	Tpm2	0.69	Atf3	0.27
Bgn	0.57	Sptbn1	0.63	Cox4i1	0.20	Timp3	0.25	Vim	0.17	Vim	0.68	Dmpk	0.27
Npc2	0.57	mt-Co1	0.63	Ank2	0.20	Canx	0.24	Ilk	0.17	Mcam	0.67	Npnt	0.27
Fuca1	0.57	Psap	0.62	Zbtb20	0.20	Smad7	0.24	Pfn1	0.17	Dmpk	0.67	Pbxip1	0.27
Selk	0.57	Rnase4	0.62	Ptma	0.20	Gnb1	0.24	Calm1	0.17	Lpp	0.66	Fblim1	0.27
Tpt1	0.57	Hexa	0.62	Dkk3	0.20	Gas6	0.24	Myh11	0.17	Bcam	0.66	Slmap	0.27
Cfh	0.56	Tpt1	0.62	mt-Co1	0.19	Itgb5	0.24	Cnn1	0.17	Col18a1	0.66	Map1b	0.27
Gabarapl1	0.56	Atp1b1	0.62	Aplp2	0.19	Serf2	0.24	Tpm1	0.17	Slmap	0.65	Clic4	0.26
Itgbl1	0.56	Lamp1	0.61	Iscu	0.19	Ank	0.24	Fxyd1	0.17	Acta2	0.64	Dnajb4	0.26
Vat1	0.56	Itgbl1	0.61	Lrp1	0.19	Ahnak	0.24	Pbxip1	0.17	Sh3bgr	0.64	Vim	0.26
Atp1b3	0.55	Lrp1	0.61	Nedd4	0.19	Bgn	0.23	Lmod1	0.17	Pdlim7	0.64	Mbnl1	0.26
Lrp1	0.55	Vat1	0.61	Klf9	0.19	Dkk3	0.23	Flna	0.16	Cald1	0.63	Filip1l	0.26
Ahnak2	0.55	Gas6	0.61	Serinc3	0.19	Rhoq	0.23	Ptgis	0.16	Ppp1r12b	0.63	Svil	0.26
Fth1	0.55	Selk	0.61	Rsrp1	0.19	mt-Co1	0.23	Cnbp	0.16	Postn	0.62	Sparcl1	0.26
Sptbn1	0.55	Abcc9	0.60	Oaz1	0.19	Nbl1	0.23	Actg1	0.16	Lmod1	0.62	Zfhx3	0.25
Atp6v0b	0.55	Cd63	0.60	Prrc2b	0.19	Selk	0.23	Ppp1r14a	0.16	Dstn	0.62	Actn4	0.25
Map1lc3b	0.55	Aplp2	0.60	Tpt1	0.19	Vat1	0.23	Rps29	0.16	Cped1	0.61	Synpo2	0.25
Itgb5	0.55	Fuca1	0.60	Lamp1	0.19	Psap	0.23	Smtn	0.16	Pfn1	0.61	Smtn	0.25
Ctsb	0.55	Cfh	0.60	Lamp2	0.19	Atp1b3	0.23	Eef1a1	0.16	Csrp1	0.61	Pcdh7	0.25
Nbl1	0.54	Gabarapl1	0.60	Bri3	0.19	Tmbim1	0.23	Myeov2	0.16	Zyx	0.61	Plcb4	0.25
Ctsd	0.54	Gpx4	0.59	Atp5l	0.19	Itgbl1	0.23	Zyx	0.16	Msrb1	0.61	Ppp1cb	0.25
Gas6	0.54	Ahnak2	0.59	Atp6v1f	0.19	Arpc1b	0.23	Mfge8	0.16	Itgb1	0.60	Dst	0.25
Rnase4	0.54	mt-Co3	0.59	Gas6	0.19	Fuca1	0.23	Atp5a1	0.16	Actn4	0.60	Ppp1r12b	0.25
Anxa5	0.54	Gns	0.59	Cox6c	0.19	Ahnak2	0.23	Rpl36	0.16	Tns1	0.60	Ptrf	0.25
Sepp1	0.54	Zbtb20	0.59	Hif1a	0.19	Malat1	0.22	Hcfc1r1	0.16	Ppp1r12a	0.60	Arid5b	0.25
Gpx4	0.54	Npdc1	0.59	Ddx5	0.19	Neat1	0.22	Sh3bgr	0.16	Hspb6	0.59	Lmod1	0.24
Mgst1	0.53	Ccdc3	0.58	Cstb	0.18	Tulp4	0.22	Naca	0.16	Npnt	0.59	Itga8	0.24
Cst3	0.53	Map1lc3b	0.58	Chchd2	0.18	Sash1	0.22	Oat	0.16	Wfdc1	0.58	Jund	0.24
Atp6ap1	0.53	Canx	0.58	Malat1	0.18	Klf9	0.22	Actn1	0.16	Susd5	0.58	Bcam	0.24
Cstb	0.53	Gpnmb	0.58	1110008P	0.18	Npdc1	0.22	Gnas	0.16	Optc	0.58	Zbtb20	0.24
Npdc1	0.53	Sepp1	0.58	Ptms	0.18	Ptp4a2	0.22	Csrp1	0.16	Cpe	0.58	Lrrfip1	0.24
Apoe	0.53	Npc2	0.58	Atp6ap1	0.18	Mprip	0.22	Rpl27	0.16	Enah	0.58	Pdlim5	0.24
Slc48a1	0.53	Itm2b	0.58	Itgb5	0.18	Ccnd2	0.22	Gapdh	0.16	Fam129a	0.58	Samd4	0.24
Gns	0.53	Sdc3	0.58	Cd63	0.18	Cfh	0.22	H3f3a	0.16	Cav1	0.58	Btg1	0.23
Atp6v1g1	0.52	mt-Co2	0.58	Oxct1	0.18	Frzb	0.22	Atp5k	0.16	Kcnmb1	0.58	Itgb1	0.23
Atpif1	0.52	Gnai2	0.58	mt-Co2	0.18	Sqstm1	0.22	Atp5c1	0.16	Cbr2	0.57	Ybx1	0.23

[A]Single-cell RNAseq analysis was performed in GFP$^+$ SMCs from thoracic aortas of tamoxifen-treated *Myh11-CreER^{T2}.mT/mG* (*n* = 2095 cells) and *Tsc1$^{fl/fl}$.Myh11-CreER^{T2}.mT/mG* (*n* = 2097 cells) mice. Gene co-expression was calculated by Spearman rank correlation and the top 50 positive correlations for selected genes are shown. In addition to molecules associated with lysosomes and autophagosomes (yellow), *Lamp2* correlated highly to Wnt signaling molecules (green). In turn, *Ctnnb1* (encoding β-catenin) showed high correlation with multiple lysosomal-related molecules. Of transcription factors that regulate lysosomal biogenesis, *Mitf* and *Tfe3* correlated with lysosomal-related and Wnt signaling molecules, whereas *Tfeb* correlated with markers of SMC differentiation (orange). Correlation coefficients for the transcription factors are lower, likely related to low abundance. To verify if our gene co-expression approach was valid, we also examined the correlation of well-characterized SMC molecules. Both *Myh11* and *Myocd* (encoding the transcription factor, myocardin) correlated with other SMC differentiation markers.

Supplemental Table 8: Characteristics of subjects and ascending aortas[A]

	Nondilated *n* = 12	Aneurysm *n* = 12	*P* value
Age (yr)	49.2 ± 14.6	60.1 ± 9.6	0.0415
Sex (% male)	58.3	100	0.0373
Race (% white)	58.3	83.3	0.3707
Height (cm)	172 ± 9.8	177 ± 9.0	0.1607
Weight (kg)	88.5 ± 20.6	95.4 ± 15.8	0.3678
Body surface area (m^2)	2.00 ± 0.25	2.12 ± 0.20	0.2090
Other aneurysms (%)	0	0	> 0.9999
Aneurysm syndrome (%)	0	0	> 0.9999
Bicuspid aortic valve (%)	0	58.3	0.0046
Family history of aneurysm (%)	0	25.0	0.2174
Known pathological mutation (%)	0	0	> 0.9999
Atherosclerosis (%)	25.0	25.0	> 0.9999
Hypertension (%)	33.3	66.7	0.2203
Dyslipidemia (%)	8.3	66.7	0.0094
Diabetes (%)	8.3	16.7	> 0.9999
Smoker (%)	83.3	41.7	0.0894
Aorta diameter (cm)	3.2 ± 0.42	5.1 ± 0.33	< 0.0001
Aorta diameter z-score	-0.17 ± 1.03	4.49 ± 1.10	< 0.0001
Media thickness (mm)	1.67 ± 0.24	1.30 ± 0.20	0.0005
Intima thickness (mm)	0.06 ± 0.04	0.10 ± 0.10	0.2609
Adventitia thickness (mm)	0.16 ± 0.15	0.08 ± 0.03	0.0927
Media area (mm^2)	157 ± 31.2	198 ± 34.0	0.0054
Medial cell density (mm^{-2})	546 ± 145	565 ± 60.3	0.6868
Media cells ($x10^3$ per section)	85.2 ± 24.3	112 ± 23.6	0.0120

[A]Ascending aorta specimens were procured from patients undergoing aortic surgery (Aneurysm) or from organ donors (Nondilated). De-identified demographic and clinical data was collected at the time of surgery; a minority of aortic aneurysm patients had undergone genetic testing. External diameter of the ascending aorta was measured from chest CT scans or with a ruler during organ procurement operations when imaging was not available. Vessel wall thickness and number of medial nuclei where determined by histomorphometry of transverse sections with total medial cell counts per aorta cross-section representing the product of medial cell density and media area. Data represent mean ± SD or %; comparisons were by t-test (continuous variables) or Fisher's exact test (categorical variables).